Development of a Two-dimensional Lithium Beam Probe for Edge Plasma Diagnostic in the Compact Helical System

Kiichiro Nakamura

Doctor of Engineering

Department of Fusion Science

School of Mathematical and Physical Science

The Graduate University for Advanced Studies

2003 (School Year)

Abstract

Diagnostics of edge plasma parameters are important because plasma properties in the region have key role to determine the global plasma confinement. In particular, transport barriers are of strong interest. Understanding and controlling edge plasmas are also important for the divertor design in fusion reactors. In order to study plasma structure in the area, two-dimensional measurements are essential.

A lithium beam probe (LiBP) is one of the best techniques for the measurement of edge plasma density profile. The LiBP utilizes the emission of the LiI resonance line (2s-2p, 670.8 nm) from the injected neutral lithium by electron impact excitation. The LiBP can probe plasmas from the edge to the core crossing the last closed flux surface (LCFS) without perturbation or contamination to the plasma. It has been used in many magnetic confinement devices, but all those measurements are in one dimensional along the fixed beam line.

A LiBP system that can measure two-dimensional plasma structure in the edge plasma region including the separatrix has been designed and installed on CHS. This system has a beam injector with variable injection angle and a multi-channel optical detection system. The beam injector is located on the upside of the torus, which consists of an ion gun with a Li source (6mm diameter) which is thermoionic emission type β-eucryptite, a Pierce extractor and cylindrical lens. This section is covered with magnetic shield in order to prevent the effect of CHS stray field. The beam energy is in the range from 10 to 20 keV with an equivalent neutral beam current of about 0.1 mA. The ion beam is neutralized in the Cs neutralizing cell operated at the temperature about 180 °C. The beam energy is selected so that it offers both adequate spatial resolution and beam penetration. For the 15 keV beam, the spatial resolution is less than 1.7 cm and beam penetration depth is characterized by the 2×10^{18} m^{-2} of line-integrated density. The neutral beam diameter is about 20 mm in the CHS vacuum chamber.

Light collection optics, which detects the emission from the LiI resonance line, is located on the side port of the torus. The optical system consists of a lens, optical fibers, optical interference filters and Avalanche Photodiode (APD) detectors. Since the angle between beam line and sight line is not at right angle, the observed spectral line suffers Doppler shift. Maximum Doppler shift at beam energy of 15 keV is 0.9 nm. So the optical interference filters are selected with the bandwidth of 2.0 nm. Twenty-five couplers for optical fibers are prepared on the light collection lens corresponding to twenty-five observation points along the beam with about 8 mm spacing. Eight channel optical fibers can select eight observation points by choosing eight couplers among those. The injection beam line angle can be varied between +18° and -18° in the major radius direction. Two-dimensional profile is obtained by changing the beam injection angle shot by shot. Since the signal to noise ratio for the present beam intensity is less than unity (S/N < 1), signals from APD detectors are introduced to phase sensitive detectors with 4 kHz beam modulation. Typical time resolution is 10 ms in the present measurements. Taking the related atomic processes into account, the emission profile is converted to the electron density profile.

The CHS is a low-aspect-ratio helical device that has a major radius of 1.0 m and minor radius of 0.2 m. The pole number and the toroidal periodic number of the helical field coils are $l = 2$ and $m = 8$, respectively. The maximum magnetic field strength is 1.8T. Magnetic field configuration can be varied over a wide range by controlling the coil current and its direction. Hydrogen plasmas are produced by electron cyclotron resonance (ECR) heating (170 kW) and additionally heated by the two neutral beam injectors (1.3 MW). The electron density is in the range of $0.5\text{-}5\text{x}10^{19}$ m^{-3} and typical electron and ion temperatures are 1 keV and several hundreds of eV, respectively. Low aspect ratio helical device characterizes broken helical symmetry due to strong toroidicity forming ergodic magnetic field line structure outside the LCFS. In CHS, variety of edge magnetic field configuration can be realized by changing the position of the magnetic axis.

Beam emission profiles are obtained both for ECH and NBI heated plasmas of limiter

configuration. Electron density is reconstructed from this emission profiles. In this study, multiple atomic processes related with transitions between 2s, 2p and ionized states are taken into account. There are two methods to convert the beam emission profile to the electron density profile. The first one is the beam attenuation method and the second one is the beam intensity method. When the plasma density is large, full emission intensity distribution is measured. Then the density profile can be reconstructed using the beam attenuation method. No calibration is necessary, which is the advantage of this method. The beam intensity method is used when the beam is not fully attenuated within the observation area. The electron density is derived from the beam emission intensity based on the atomic data, sensitivity of the optical system and the beam density. Two-dimensional electron density profiles are derived using those two methods depending on the beam penetration depth..

The experimental data suggests that the ECH plasma is well confined inside the LCFS. Plasmas with density above 10^{18} m^{-3} do not exist outside of it. In contrast, the NBI plasma is spreading outside the LCFS toward the separatrix region and noticeable amount of plasma is confined in this ergodic region even though the magnetic field line in the ergodic layer is cut by the vacuum chamber wall (inboard limiter configuration). The plasma with the density of 10^{19} m^{-3} exists even 4 cm apart from the LCFS along the equatorial plane.

Edge density profile steeping associated with H-mode like transitions (Edge Transport Barrier) is also observed. The characteristic scale length of the electron density gradient at the LCFS is reduced to 80 % of the original one.

Such 2D-diagnostics is expected to play a key role in understanding and the design of helical diverter in future.

Contents

List of Figures

Chapter 2

Chapter 3

Chapter 4

1. Introduction

Determination of plasma parameters at the edge region of magnetic fusion devices has become an important issue because plasma properties in the region have key role to determine the global plasma confinement. In particular, transport barriers are of strong interest. In 1982, H-mode discharge was found in NBI heated plasma with divertor configuration in ASDEX Tokamak [1.1]. After that, H-mode has been observed in many other divertor tokamaks. In 1990, H-mode was also found with limiter configuration in JIPPT-IIU Tokamak [1.2]. In stellarator type devices, H-mode was found on 1993 both in CHS [1.3] and Wendelstain 7-AS [1.4].

In H-mode discharges, transport barriers with steep electron temperature and density gradients are formed inside the last closed flux surface (LCFS). And then, plasma density increases in the edge region and energy confinement time is improved compared with the normal discharges (L-mode). Characteristic phenomenon in H-mode plasma called Edge Localized Mode (ELM) is also observed. There are many topics, which are not yet solved about the H-mode physics.

Understanding and controlling edge plasmas are also important from the point of view of the divertor design for fusion reactors. Edge plasma has a role of buffer layer between core plasma and divertor. In order to reduce thermal loading on the divertor plates, lower edge plasma temperature is expected, which also decrease impurities from chamber wall. In non-axisymmetric helical devices, edge magnetic configurations intrinsically include ergodic layer and magnetic island structures. A helical device like the Large Helical Device (LHD) or the CHS has toroidally continuous natural divertor similar to double-null X point structure in tokamaks. However the magnetic lines of force in this region play chaotic behavior forming ergodic region. The separatrix is not clear as that in tokamaks. The role of the ergodic layer such as the screening of impurities and fuel neutral particles has been discussed, but no clear physical picture is obtained. It is important to measure the plasma distribution and its parameters in this

layer.

Measurement of plasma density in the separatrix region is also important from the diagnostic point of view. Core plasma density profile is often determined by Abel inversion of multi-channel interferometers. In the case of heliotron type device, the chord inevitably passes the separatrix region. Ambiguity of electron density in this region affects the accuracy of core density profile determination. In order to study plasma structure in this area, two-dimensional measurements are essential.

There are many diagnostic techniques to measure physical quantities in edge and diverter plasmas. Langmuir probe method is the technique to measure plasma potential, electron density, electron temperature, and ion density by means of small electrode insertion into plasmas [1.5]. Various types of electrodes have been developed depending on their purposes. A double probe, a triple probe and an emissive probe are examples. In addition, an ion sensitive probe for ion temperature measurement and a Mach probe for plasma flow velocity measurement are also used. Since Langmuir probes are simple to treat and are less expensive, they have been widely used in many fusion devices. However, they have disadvantages such as disturbance to plasmas and source of impurities. A magnetic probe is used to measure magnetic field fluctuations in the edge plasmas. Mirnov coils are a set of magnetic probes for the measurement of mode number of edge MHD oscillations.

Optical diagnostic methods combined with probing neutral beams can also be used to measure edge plasmas but deeper into the core region. Beam emission spectroscopy using heating beams is the method to measure ion density fluctuations. Charge exchange spectroscopy is used to measure ion temperature via Doppler broadening and plasma rotation via Doppler shift of impurity spectral lines. Electric field measurement by the use of Stark effect [1.6 - 1.8] and magnetic field measurement by the use of Zeeman [1.9 - 1.13], are other examples of this type of diagnostics. A heavy ion beam probe (HIBP) is so far considered as a core plasma diagnostic method [1.14], but for present day large size plasmas, it can be used as a diagnostic of edge plasmas such as for H-mode studies.

Thomson scattering method is another powerful diagnostic for edge and diverter plasmas. It provides local electron temperature and density with high spatial and temporal resolution. Recently the method is extended to two-dimensional measurement around the X-point of tokamak plasmas [1.15].

Among those various diagnostics, a lithium beam probe is (LiBP) is one of the best techniques for the measurement of edge plasma density profile. This method, which utilizes the emission of the injected neutral lithium beam by electron impact excitation was developed by Kadota et al.. The LiBP can probe plasmas from the edge to the core crossing the last closed flux surface (LCFS) without perturbation or contamination to the plasma. It has been used in many magnetic confinement devices. But all those measurements are in one dimensional along the fixed beam line.

In this thesis, a new LiBP diagnostic system is described which has been developed to measure two-dimensional plasma structure in the edge plasma region including the separatrix of the CHS helical device. This system has a beam injector with variable injection angle and a multi-channel optical detection system. Changing the beam injection angle shot by shot, two-dimensional beam emission profile is obtained. Taking the related atomic processes into account, the emission profile is converted to the two-dimensional electron density profile in the edge region of CHS plasma. Edge density profile steeping associated with H-mode like transitions is also observed with this method.

2. Development of two-dimensional Li beam probe

2.1 Review of LiBP

Plasma density measurement using a particle beam was first developed by H. P. Eubank et, al in 1965, who used atomic hydrogen beam to measure the plasma ion density on B-1 stellarator [2.1]. They obtained line-integrated density $<n_e l>$ using beam attenuation. R. Hickok used 1 MeV H_2^+ beam to measure plasma density and its fluctuation, where dissociated H^+ beam was detected [2.2]. This method was further developed and extended to the first heavy ion beam probe using a thallium beam as space potential diagnostic for the ST tokamak [2.3].

A lithium beam probe is first proposed by J. Fujita and K. McCormick as a method of current profile measurements via the Zeeman effect in a tokamak [2.4]. K. Kadota et al, proposed that the lithium beam can be used for plasma density measurement, and demonstrated the proof of principle experiment in a small ECR plasma in 1978 [2.5]. Then, Iguchi et al, used a 4 keV 10-30 μA beam in NBT-1M and measured plasma density in the range of 10^{17} m^{-3} [2.6]. In this study, beam attenuation by collisions with plasma particles was neglected, and simple relation that emission intensity of the Li I resonance line is proportional to plasma density is used. It is a reasonable assumption for such low density plasmas. But in a high density plasma ($>10^{18}$ m^{-3}), beam attenuation becomes severe. Then, a higher energy lithium beam (60 keV 0.5 mA) was used to get larger penetration depth in ASDEX [2.7,8]. In this case, the spatial resolution was considered to be worse because of finite lifetime of the lithium-excited state. Moreover, the density reconstruction procedure becomes more complicated. Charge transfer from Li atoms to plasma protons and impurity ions become dominant for the beam attenuation. On the other hand, a 15 keV Li beam was used in TEXTOR to measure radial profiles of impurity ion concentrations (e.g. He, C, O) via charge exchange recombination spectroscopy [2.9]. In this way, diagnostics using lithium beam

became popular in higher density plasmas. However, in a high density plasma, atomic processes become complicated and a full collisional radiative model is required for the electron density profile reconstruction. Excitation, ionization and charge exchange by plasma ions as well as by electrons have to be taken into account. In 1991, recursive algorithm to reconstruct the plasma electron density is developed by J. Schweinzer et al., and the applicability of this algorithm was illustrated in TEXTOR (20 keV, 5-10 mA) [2.10]. This technique can derive an absolute density profile from the beam emission profile without absolute calibration of the detector system. The technique was improved and applied to W7-AS (48 keV, 1.5 mA) [2.11] where the spatial resolution of about 0.5 cm and time response of less than 0.2 ms are obtained [2.12]. In the CHS, electron density measurements were carried out using a 8 keV beam (50 μA) [2.13-15]. On the contrary, in the TEXT, 20-30 keV, 1-2 mA beams were used, where the signal to noise ratio was improved by measuring the lithium beam emission and plasma background light [2.16]. Moreover, also in JET [2.17] and LHD [2.18], LiBPs are recently installed (using a 50 keV beam and a 30 keV beam respectively), and new results are being produced.

On the other hand, an LiBP is also used for diagnostic other than plasma density. In DIII-D, a lithium beam (10-30 keV, 5-10 mA) is used to measure edge density fluctuations $\tilde{n}/n_0$ for H-mode plasmas [2.19]. Recently, it is also used to measure poloidal magnetic field via the Zeeman splitting [2.20].

As mentioned above, a higher energy lithium beam has been used in many recent magnetic confinement devices.

2.2 Principle of LiBP

2.2.1 Atomic process

The atomic lithium, the lightest alkali metals whose atomic number is 3 ($1s^2 2s$), has

only one electron in L-shell which is outside the filled K-shell, that is, it is similar to a hydrogen-like atom in spectroscopic sense. Because of rather simple spectral line structure, interpretation of the spectral line intensities or the line profiles to plasma parameters to be measured is not difficult. In addition, the lithium atom has a strong resonance line ($1s^2 2s - 1s^2 2p$) in the visible wavelength range (670.8 nm). Standard optical components such as glass lens, optical fibers and photo-detectors are available and can be arranged outside the vacuum chamber, which is an advantage for beam probe spectroscopy. It is in contrast with the helium atom, whose electron structure is also simple but the strong spectral lines are in vacuum ultra-violet range.

The energy level diagram for the lithium atom is shown in Fig. 2.1. The Li I resonance line is associated with the transition from 2p to 2s (LiI: 670.8 nm). Since the life time of the 2p state is short (26.9 ns), the emission intensity is proportional to the number density of the lithium atom in 2p state, which depends on various atomic processes such as collisional impact excitation by electrons and ions, and charge exchange with ions.

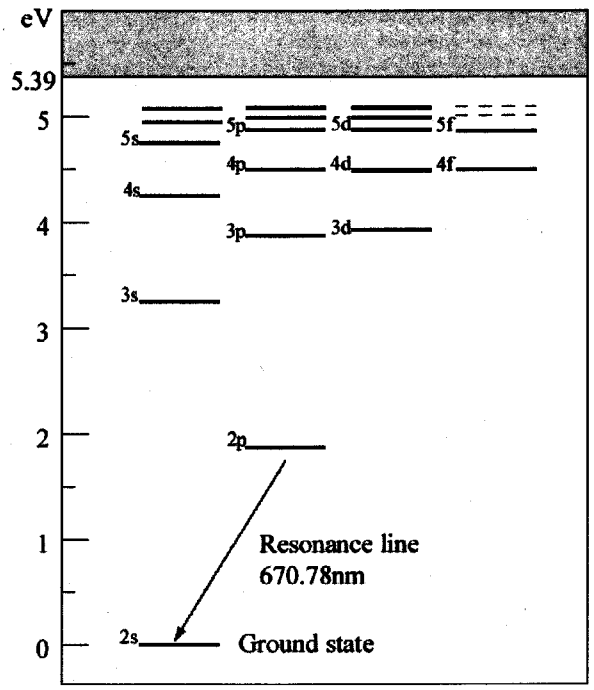

Fig. 2.1 Energy Level Diagram of the Li Atom

The lithium beam penetration length is determined by the attenuation of the injected beam, which is the measure of the observable depth from the plasma edge. It is caused by ionization through electron and ion impact and charge exchange with plasma ions. The penetration length depends on the injected beam energy as well as target plasma parameters. These processes are expressed as follows:

Electron impact ionization	$(Li + e \rightarrow Li^{+} + 2e)$
Ion impact ionization	$(Li + H^{+} \rightarrow Li^{+} + H^{+} + e)$
Charge exchange	$(Li + I^{Z+} \rightarrow Li^{+} + I^{(Z-1)+})$

where hydrogen plasma is assumed. The notation I represents ion species including impurities and Z is their charge. The ionization or charge exchange rate coefficients depend on relative velocities between lithium atoms and target plasma particles. When the beam energy is less than 10 keV and the ion temperature is less than 1 keV, the dominant loss process is electron impact ionization. But when the beam energy or the ion temperature is higher, ionization processes by ion impact or charge exchange become important.

On the other hand, excitation processes for the lithium atoms are expressed as follows:

Electron impact excitation	$(Li + e \rightarrow Li^{*} + 2e)$
Ion impact excitation	$(Li + H^{+} \rightarrow Li^{*} + H^{+})$
Charge exchange	$(Li + I^{Z+} \rightarrow Li^{*} + I^{(Z-1)+})$
Photoexcitation	$(Li + h\nu \rightarrow Li^{*})$

where * indicates an excited state. Rate coefficients for those excitation processes are generally larger than those for ionization processes by an order of magnitude. But their dependences on the beam or plasma particle energies are similar.

2.2.2 Effective rate coefficients

Electronic transition processes for the Li atom are schematically shown in Fig. 2.2. Here $\langle\sigma_{ex}v_{r\text{-}e}\rangle$ is the excitation rate coefficient by electron impact and $\langle\sigma_{ex}v_{r\text{-}i}\rangle$ is by ion impact. $\langle\sigma_{dex}v_{r\text{-}e}\rangle$ is the deexcitation rate coefficient by electron impact and $\langle\sigma_{dex}v_{r\text{-}i}\rangle$ is by ion impact. $\langle\sigma_{is}v_{r\text{-}e}\rangle$ is the ionization rate coefficient from ground state by electron impact, $\langle\sigma_{is}v_{r\text{-}i}\rangle$ is by ion impact and $\langle\sigma_{cs}v_{r\text{-}i}\rangle$ is by charge exchange. Then $\langle\sigma_{ip}v_{r\text{-}e}\rangle$ is the ionization rate coefficient from p state by electron impact, $\langle\sigma_{ip}v_{r\text{-}i}\rangle$ is by ion impact and $\langle\sigma_{cp}v_{r\text{-}i}\rangle$ is by charge exchange.

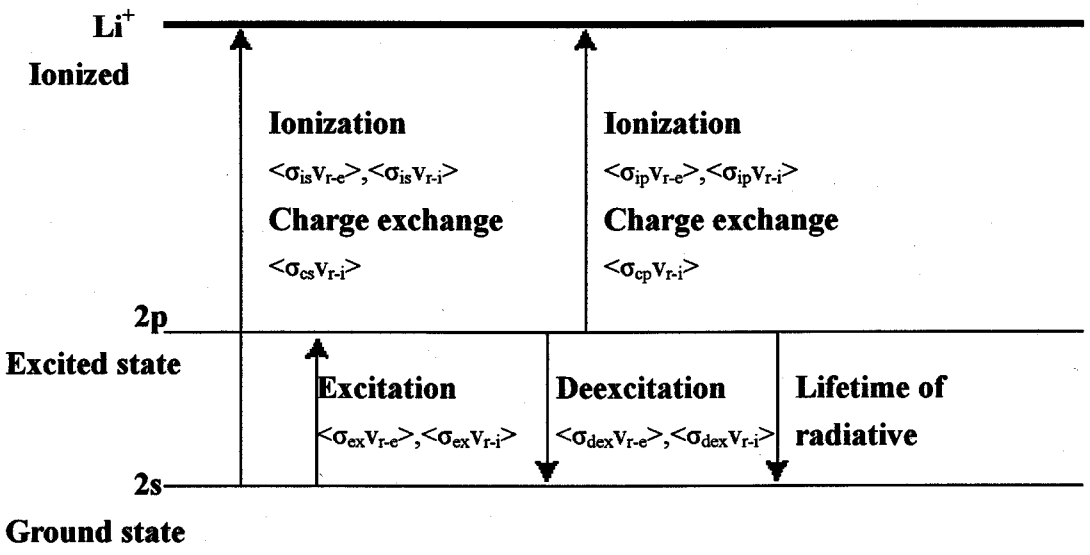

Fig 2.2 Atomic processes of Li atom in collision with plasma particles.

The values of those rate coefficients are found in reference 2.13, 2.21-2.22. The electron temperature dependence of the rate coefficients $<\sigma_{ex}v_{r-e}>$, $<\sigma_{dex}v_{r-e}>$, $<\sigma_{is}v_{r-e}>$ and $<\sigma_{ip}v_{r-e}>$ are shown in Fig. 2.3. Here, v_{r-e} is the relative electron velocity and v_{r-i} is the relative ion velocity with respect to the lithium beam.

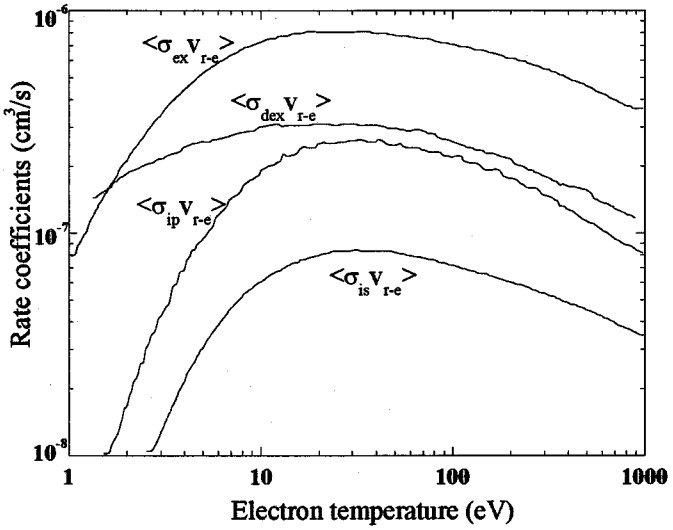

Fig. 2.3 Electron temperature dependence of the effective rate coefficients.

In order to simplify the analysis for the density profile reconstruction, the idea of effective rate coefficients are introduced.

In the collisional radiative model, the rate equation for the excited state of the Li atom (2p) is expressed as follows:

$$\frac{dn_{\text{Li-p}}}{dt} = n_e < \sigma_{ex} v_r > n_{\text{Li-s}} - n_e < \sigma_{dex} v_r > n_{\text{Li-p}} - n_e < \sigma_{ip} v_r > n_{\text{Li-p}} - \frac{n_{\text{Li-p}}}{\tau_{em}} = 0 \quad (2.1)$$

where the $<\sigma_{ex}v_r>$ is the rate coefficient for excitation from 2s to 2p excitation. $<\sigma_{dex}v_r>$ is the rate coefficient of deexcitation process and $<\sigma_{ip}v_r>$ is the rate coefficient of

ionization process from 2p state. The n_e, $n_{Li\text{-}p}$ and $n_{Li\text{-}s}$ are densities of the electron, excitated state Li atom and grand state Li atom, respectively, and τ_{em} is the lifetime of radiative transition from 2p state (26.9 ns), which is a reciprocal of transition probability As-p.

These rate coefficients include the effects both from the electron and the ion. They are defined as follows

$$<\sigma_{ex} v_r >= <\sigma_{ex} v_{r\text{-}e} > + <\sigma_{ex} v_{r\text{-}i} > \tag{2.2}$$

$$<\sigma_{dex} v_r >= <\sigma_{dex} v_{r\text{-}e} > + <\sigma_{dex} v_{r\text{-}i} > \tag{2.3}$$

$$<\sigma_{is} v_r >= <\sigma_{is} v_{r\text{-}e} > + <\sigma_{is} v_{r\text{-}i} > + <\sigma_{cs} v_{r\text{-}i} > \tag{2.4}$$

$$<\sigma_{ip} v_r >= <\sigma_{ip} v_{r\text{-}e} > + <\sigma_{ip} v_{r\text{-}i} > + <\sigma_{cp} v_{r\text{-}i} > \tag{2.5}$$

The ratio of $n_{Li\text{-}p}$ to $n_{Li\text{-}s}$ is calculated from eq. (2.1) and is expressed as

$$\frac{n_{Li\text{-}p}}{n_{Li\text{-}s}} = \frac{n_e <\sigma_{ex} v_r > \tau_{em}}{1 + n_e \{<\sigma_{ex} v_r > + <\sigma_{ip} v_r >\} \tau_{em}} \tag{2.6}$$

Here, the effective emission rate coefficient $<\sigma_{em} v_r>_{eff}$ for LiI resonance line (2p-2s) is defined as follows

$$\frac{n_{Li\text{-}p}}{\tau_{em}} = n_e <\sigma_{em} v_r >_{eff} n_{Li} , \tag{2.7}$$

where n_{Li} is the total Li density $n_{Li} = n_{Li\text{-}s} + n_{Li\text{-}p}$. Substituting eq. (2.6) into eq. (2.7), $<\sigma_{em} v_r>_{eff}$ can be deduced to

$$<\sigma_{em} v_r >_{eff} = \frac{<\sigma_{ex} v_r >}{1 + n_e \{<\sigma_{dex} v_r > + <\sigma_{ip} v_r > + <\sigma_{ex} v_r >\} \tau_{em}} . \tag{2.8}$$

In the same way, the effective ionization rate coefficient $<\sigma_i v_r>_{eff}$ for Li atom can be defined as follows:

$$n_e < \sigma_i v_r >_{eff} n_{Li} = n_e < \sigma_{is} v_r > n_{Li\text{-}s} + n_e < \sigma_{ip} v_r > n_{Li\text{-}p} \quad (2.9)$$

Then $<\sigma_i v_r>_{eff}$ is written as follows:

$$< \sigma_i v_r >_{eff} = \frac{< \sigma_{ex} v_r > + n_e \{ < \sigma_{is} v_r >< \sigma_{ip} v_r > + < \sigma_{is} v_r >< \sigma_{dex} v_r > + < \sigma_{ip} v_r >< \sigma_{ex} v_r > \} \tau_{em}}{1 + n_e \{ < \sigma_{dex} v_r > + < \sigma_{ip} v_r > + < \sigma_{ex} v_r > \} \tau_{em}} \quad (2.10)$$

The density dependence of these effective rate coefficients are shown in Fig. 2.4.

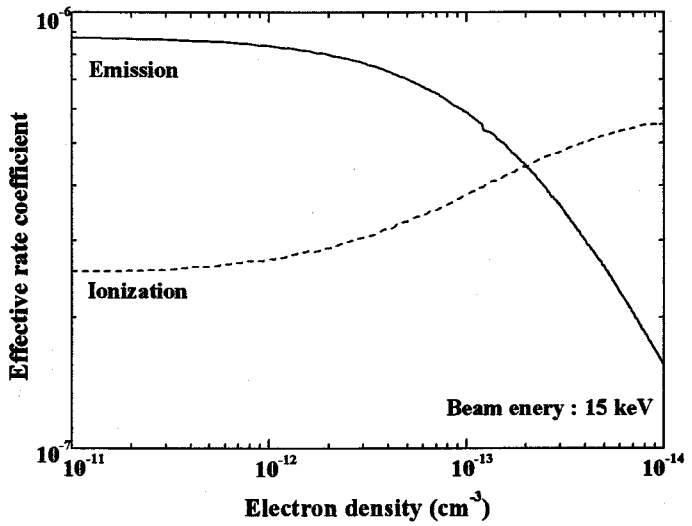

Fig. 2.4 Electron density dependence of the effective rate coefficients at beam energy of 15 keV.

2.2.3 Density profile reconstruction

Lithium atoms injected into plasmas are excited by collisions with plasma particles and emit photons in series of spectral lines. The intensity of LiI resonance line

(2p-2s/670.8 nm) is the strongest one among them. Let us consider the situation to detect those photons with an optical system of solid angle Ω, sampling volume V and efficiency η. The number of photons $N_{vp}(x)$ to be detected is described as

$$N_{vp}(x) = n_e(x)\, n_b(x) \langle \sigma_{em} v_r \rangle_{eff} \Omega/4\pi V\eta \qquad (2.11)$$

where, $n_e(x)$ is the electron density, $n_b(x)$ is the lithium atom density, $\langle \sigma_{em} v_r \rangle_{eff}$ is the effective emission rate coefficient of the resonance line, and x is the distance along the beam. Here v_r is the relative velocity between plasma particles and lithium atom.

In general, the LiBP is used for edge plasmas where electron and ion temperatures are less than a few hundred eV. Since the temperature dependence of the rate coefficient for electron impact excitation is very week in the range from 10 eV to a few hundreds eV, it is usually assumed to be constant. This assumption is broken when electron temperature becomes less than10 eV. The rate coefficient for the ion impact excitation is also constant because relative velocity is determined by the lithium beam velocity in this temperature range. The effective emission rate coefficient described in eq. (2.8) includes both contributions. The beam density is also a function of the location in the plasma, because it suffers attenuation due to ionization and charge exchange processes. Then the unknown parameters in the equation (2.11) are $n_e(x)$ and $n_b(x)$. The eq.(2.11) is rewritten as follows

$$n_e(x) = \frac{N_{vp}(x)}{n_b(x)\langle \sigma_{em} v_r \rangle_{eff} \Omega/4\pi V\eta} \qquad (2.12)$$

In the region that plasma density is small and beam attenuation is negligible, the beam emission intensity is proportional to the electron density. In this case, the eq. (2.12) can simply be written as

$$n_e(x) = \frac{N_{vp}(x)}{n_b(0)\langle\sigma_{em}v_r\rangle_{eff}\Omega/4\pi V\eta} = \frac{\alpha}{\langle\sigma_{em}v_r\rangle_{eff}}N_{vp}(x) \qquad (2.13)$$

Here $\alpha = 1/n_b(0)\Omega/4\pi V\eta$ is a proportional constant. Then the electron density profile simply coinsides the beam emission profile.

When the beam attenuation is not negligible, which is usually the case, there are two methods to convert the beam emission profile to the electron density profile. The first one is the beam attenuation method and the other is the beam intensity method.

a) Beam attenuation method

When the beam is fully attenuated within the observation area, beam attenuation method can be used. Electron density $n_e(x)$ is determined by integrating the $N_{vp}(x)$ from the position x toward the emission tail-off position x_1.

Beam attenuation due to ionization is express as

$$\frac{1}{n_b(x)}\frac{dn_b(x)}{dx} = -n_e(x)\frac{\langle\sigma_{ion}v_r\rangle_{eff}}{v_b}. \qquad (2.14)$$

Where $\langle\sigma_{ion}v\rangle_{eff}$ is the effective ionization rate coefficient and v_b is the lithium beam velocity. Then the beam density is described as

$$n_b(x) = n_{b0}\exp\left(-\int_0^x n_e(l)\frac{\langle\sigma_{ion}v_r\rangle_{eff}}{v_b}dl\right). \qquad (2.15)$$

Solving for $n_e(x)$ in equation (2.11), and substituting it into equation (2.15), finally integrating from x to x_1, the beam density $n_b(x)$ is alternatively expressed as

$$n_b(x) = -\int_x^{x_1} \frac{dn_b(l)}{dl} dl = \int_x^{x_1} \left[N_{vp}(l) \frac{<\sigma_{ion} v_r>_{eff}}{<\sigma_{em} v_r>_{eff}} \Big/ (\Omega/4\pi) V \eta v_b \right] dl . \quad (2.16)$$

Combining equations (2.11) and (2.16), the electron density now can be expressed as

$$n_e(x) = \frac{N_{vp}(x) v_b}{\langle \sigma_{em} v_r \rangle_{eff}} \Big/ \int_x^{x_1} N_{vp}(l) \frac{\langle \sigma_{ion} v_r \rangle_{eff}}{\langle \sigma_{em} v_r \rangle_{eff}} dl . \quad (2.17)$$

Now the electron density profile is determined by the ratio of the local beam emission intensity and its integration from the emission tail-off position (beam attenuation position) to the observation point. No calibration is necessary, which is the advantage of this method.

Since the ratio $<\sigma_{ion} v_r>_{eff} / <\sigma_{em} v_r>_{eff}$ is a function of the electron density, iteration process is necessary to obtain the electron density profile. Assuming the ratio at the low density limit to be constant and giving it as an initial value, the starting density profile for iteration can simply be obtained as

$$n_e(x) = \frac{N_{vp}(x) v_b}{\langle \sigma_{ion} v_r \rangle_{eff}} \Big/ \int_x^{x_1} N_{vp}(l)\, dl \quad (2.18)$$

Then the final density profile is calculated from eq. (2.17) by iteration.

b) Beam intensity method

The other method is the beam intensity method, which can be used when the beam is not fully attenuated within the observation area. The electron density $n_e(x)$ is derived from the beam emission intensity $N_{vp}(x)$ based on the atomic data, sensitivity of the optical system and the beam density $n_b(x)$.

For a given density profile initially, the emission intensity $N_{vp}(x)$ can be calculated numerically using the equations (2.11) and (2.15), which is denoted as $N^*_{vp}(x)$ here. It is written in terms of the constant α defined in eq. (2.13) as

$$N^*_{vp}(x) = n_e(x)\frac{\langle \sigma_{em} v_r \rangle_{eff}}{\alpha} \exp\left(-\int_0^x n_e(l)\frac{\langle \sigma_{ion} v_r \rangle_{eff}}{v_b} dl \right). \tag{2.19}$$

The electron density is determined by iteration so that the observed emission intensity $N_{vp}(x)$ coincides with the numerically calculated $N^*_{vp}(x)$.

In general, the constant α can be determined by a calibration method using a gas target. When the lithium beam is injected into a uniform gas target (for example He) with known pressure, the observed emission intensity $N_{vg}(x)$ is written as

$$N_{vg}(x) = n_g(x)\, n_{b0} \sigma^g_{ex} v_b\ \Omega/4\pi \mathrm{V}\eta \tag{2.20}$$

Where n_g is the target gas atom number density, σ^g_{em} is the cross section for the 2s-2p excitation due to collision with lithium and target gas particle and v_b is the beam velocity. Then the constant α can be obtained as follows:

$$\alpha = n_g \sigma^g_{ex} v_b / N_{vg} \tag{2.21}$$

In this case absolute values of the collisional excitation cross section and number density of the target gas have to be given [2.5].

Alternatively the α can be given experimentally using the beam attenuation method, which method is adopted in this paper and will be described in section 3.3.

2.3 Preparation of Neutral Li beam

Neutral Li beam is developed at a beam probe test stand, which is shown in figure 2.5. The ion beam is generated and accelerated in the gun part. Then ion beam is neutralized in a cesium neutralizer. The beam current is measured by a Faraday cup type beam current detector that is set at the end of the camber. A β-eucryptite ($Li_2O•Al_2O_3•2SiO_2$) lithium ion source which is thermionic emission type, is used [2.23]. M. Ueda. et al, has shown that the β-eucryptite in grassy state emits 8-10 times more ions than that in the pasty state. The life time is twice longer as well [2.24]. So glassy state β-eucryptite is used. It is made frpm powder state β-eucryptite by heating it up to 1300 C° in vacuum.

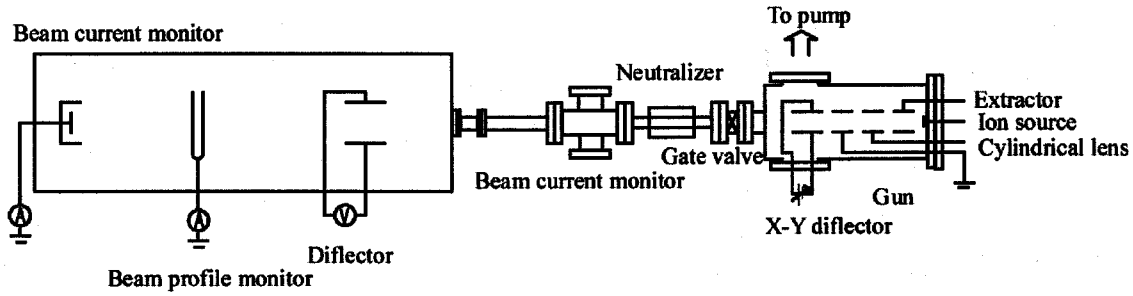

Fig 2.5 Experimental setup for Li beam development at the testsatnd.

The lithium ion Li^+ is extracted by the Pierce extractor and accelerated and focused by cylindrical lens. Figure 2.6 shows the relationship between extraction voltage and beam current. The fitting line in this figure suggests that the 3/2 power low is realized between extraction voltage and ion beam current [2.5]. The Li^+ beam is neutralized in the Cs vapor in a neutralizing cell. Cesium is an alkali metal and charge exchange cross section between alkali metals is large even for different atom species. The advantage using cesium is that the operation temperature is low compared with other alkali metal

vapors (sodium 240 C°, lithium 500 C°). So heating from outside of the vacuum chamber by the use of a simple heater wire is available. Figure 2.7 shows the neutralizing efficiency as a function of the oven temperature. It shows that the ion beam is almost neutralized at about 180 C°.

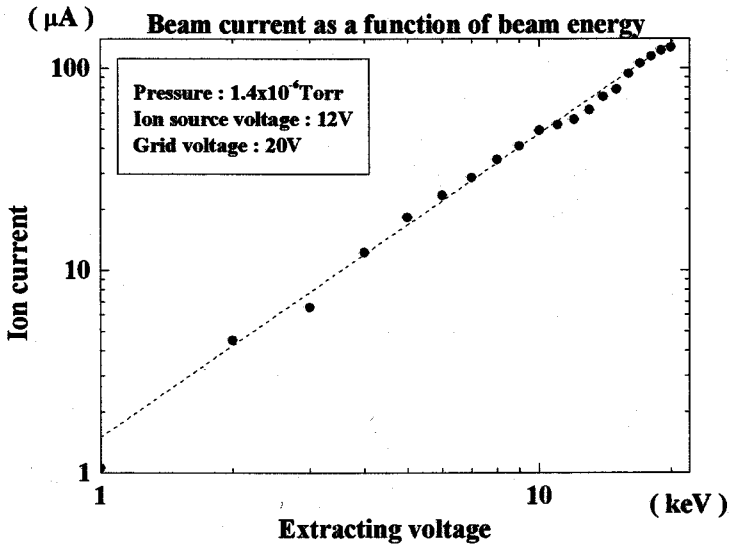

Fig 2.6 Experimental result of the relationship between extraction voltage and beam current. Broken line is theoretical dependence of 3/2 power low in the of space charge limited region.

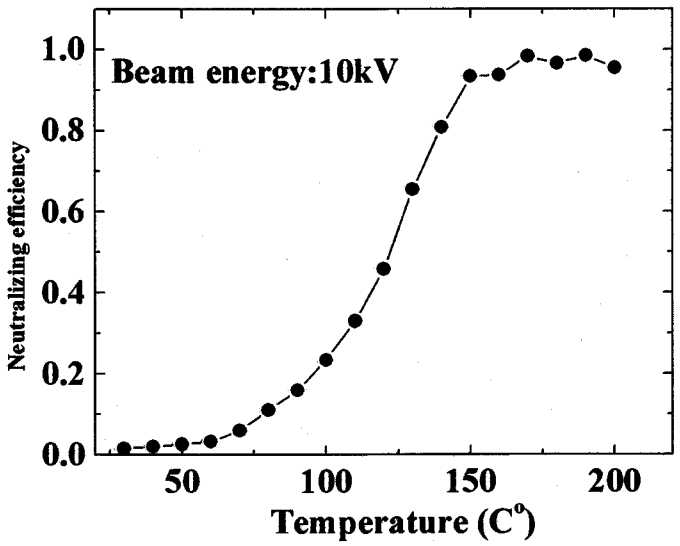

Fig 2.7 Experimental result of neutralizing efficiency as a function of the cesium oven temperature.

3. Two-dimensional measurements on the CHS

3.1 CHS device

3.1.1 Device parameter

The CHS is a low-aspect-ratio helical device that has a major radius of 1.0 m and averaged minor radius of 0.2 m which gives a plasma aspect ratio A_p of 5. Layout of the CHS main chamber, heating and diagnostic systems are shown in Fig 3.1. The pole number and the toroidal periodic number of the helical field coils are $l = 2$ and $m = 8$, respectively [3.1-3.3]. The maximum magnetic field strength is 1.8T. Magnetic field configuration can be varied over a wide range by controlling three pairs poloidal coils with the coil currents and its direction. This flexibility is useful for studying the helical plasma confinement. A hydrogen plasma is produced by electron cyclotron resonance (ECR) heating with a 53.2 GHz, 200 kW gyrotron. The plasma is additionally heated by the two neutral beam injectors (NBI / 40 keV with total power of 1.8 MW). The electron density is in the range of 0.5 - 5 x 10^{19} m^{-3} and typical electron and ion temperatures are 1 keV and several hundreds of eV, respectively. The electron line density is measured by a 2mm microwave interferometer [3.4,5]. The electron temperature and electron density profiles are measured by a YAG laser Thomson scattering [3.6]. The ion temperature is measured by a charge exchange recombination spectroscopy (CXRS) [3.7].

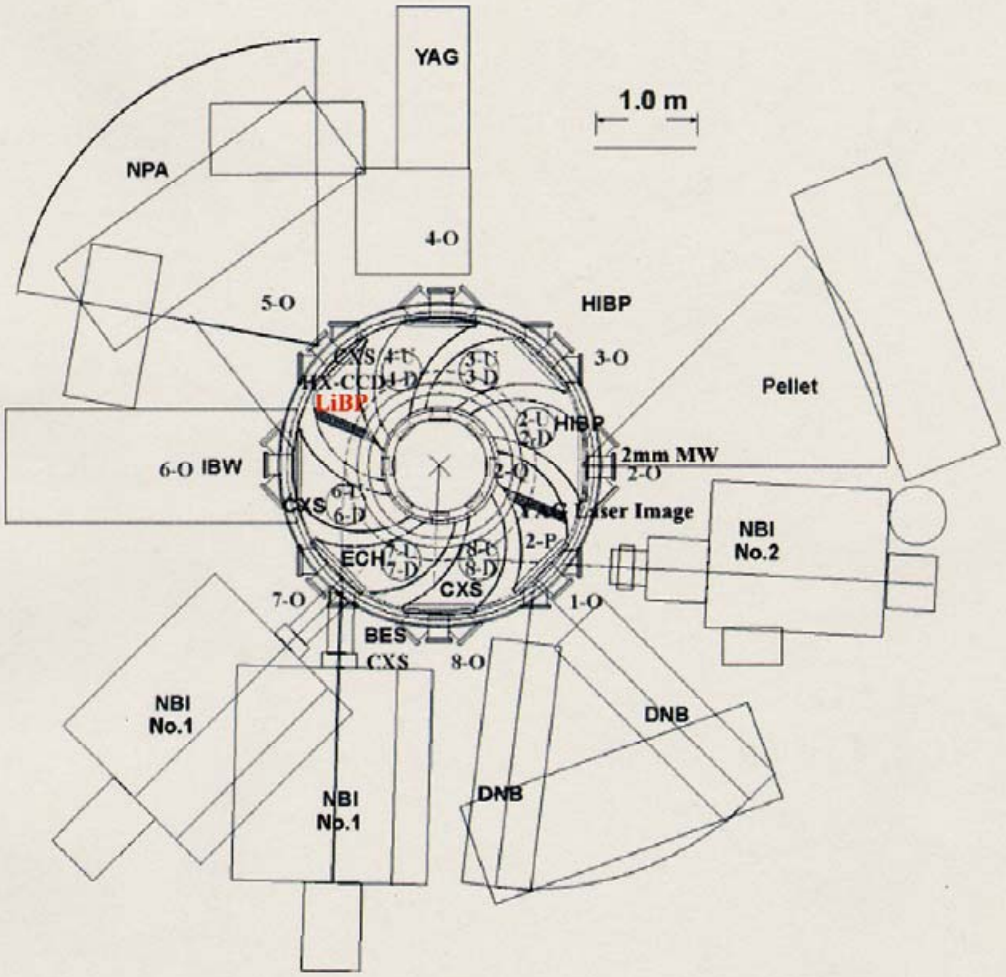

Fig 3.1 Layout of the heating and diagnostic systems on CHS.

3.1.2 Field line structure

A Low aspect ratio helical device characterizes broken helical symmetry due to strong toroidicity forming ergodic magnetic field line structure outside the last closed flux surface (LCFS). The toroidal ripple in magnetic field strength ε_t is about 0.2 and is comparable to the helical ripple ε_h near the plasma edge. In CHS, variety of edge magnetic field configuration can be realized by changing the position of the magnetic axis.

The field line structures in the edge region are calculated for two typical magnetic configurations. Figure 3.2(a) and (b) show the Poincare plots of the magnetic field line outside the LCFS on a poloidal cross section for R_{ax} = 0.921 m and R_{ax} = 0.995 m, namely, the inboard limiter case and the magnetic limiter case. Each configuration is realized by inward-shifted or outward-shifted magnetic axis, respectively. It is noted that the starting points of the field line trace is uniformly distributed outside the LCFS and the plotted points are the superposition of the points on poloidal cross section at every 45 degree in toroidal direction reflecting the m number of 8. The field line trace is terminated if it crosses the vacuum chamber wall. These figures qualitatively provide the image of the field line ergodicity outside the LCFS, although it is not a direct indication of the field line connection length to the wall.

Normal operational configuration in the CHS is the inward-shifted one at R_{ax} = 0.921 m, in which plasma performance is generally maximized. In this case the inboard wall at eight positions in the toroidal direction plays a role of material limiter, making the connection length outside of the LCFS very short. The ergodic layer disappears, which is in contrast to the outward-shifted configuration. Flexibility having such variety in edge magnetic field configuration is an advantage of CHS device for the present study.

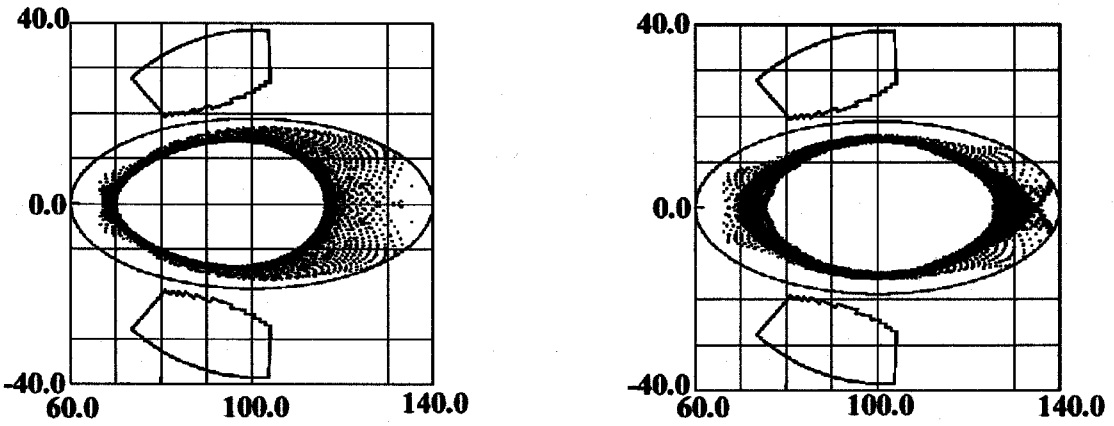

Fig 3.2 Poincare plots of the magnetic field line on a poloidal cross section (every 45° in toroidal direction) outside the LCFS for (a) R_{ax} = 0.921 m and (b) R_{ax} = 0.995 m

3.1.3 Transport barrier

In CHS, H-mode is found first for the plasma with co-direction ohmic current in 1993 [3.8]. It was also found about the same time in Wendelstain 7-AS [3.9]. These are the first observations of H-mode in stellarator type devices and are recognized as a start point of the studies of various improved confinement modes in stellerators. Recently in LHD, H-mode discharge is also found in the low magnetic field [3.10].

The main topics of the improved confinement study in CHS is the neoclassical internal transport barrier (N-ITB) which is a unique feature of stellarator type devices. The edge transport barrier (ETB) is the next topic for the total confinement improvement. The ETB for the particle transport is found recently in the NBI heated plasmas. This ETB is characterized by the clear drop of Hα emissions and the appearance of the back transition when the heating power decrease below the power threshold. No ohmic current drive is necessary. Its transition and back transition are controlled by the heating power [3.11].

3.2 Experimental set up

The 2D-LiBP system has been installed on the CHS as shown in Fig. 3.3. The coordinate system used here is defined as follows. The x-axis is taken same as the major radius on the equatorial plane measured from the toroidal axis y. The x-y plane is defined on the poloidal cross section where beam injection and detection optics are located. The system consists of two parts. One is a beam injection part that generates and injects the neutral Li beam. The other is an optical detection part that observes light emission from the injected Li beam by the collision with plasma particles.

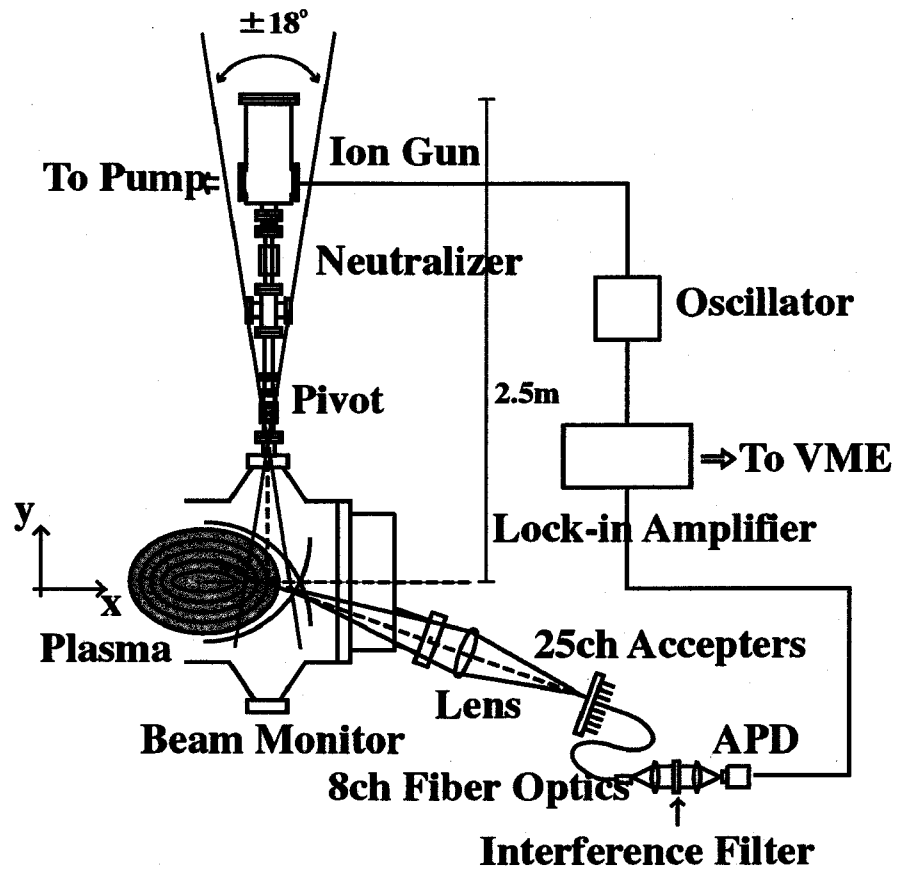

Fig 3.3 Experimental setup for the 2D-LiBP system on CHS. Two-dimensional profile is obtained by changing the beam injection angle shot by shot.

3.2.1 Beam injection part

The Li-beam injector is located on the upside of the torus (5M port). The injector consists of an ion gun with a Li source (6mm diameter) which is thermoionic emission type β-eucryptite, a Pierce extractor, cylindrical lens and X-Z deflector plates, where z is the toroidal direction. This section is covered with magnetic shield in order to prevent the effect of CHS stray field. Figure 3.4 shows a schematic drawing of the beam gun. Li ion beam is extracted from the source and accelerated and focused by Pierce gun and cylindrical lens. The beam energy is in the range from 10 to 20 keV with an equivalent neutral beam current of about 0.1 mA. The beam energy is selected so that it offers both an adequate spatial resolution and beam penetration.

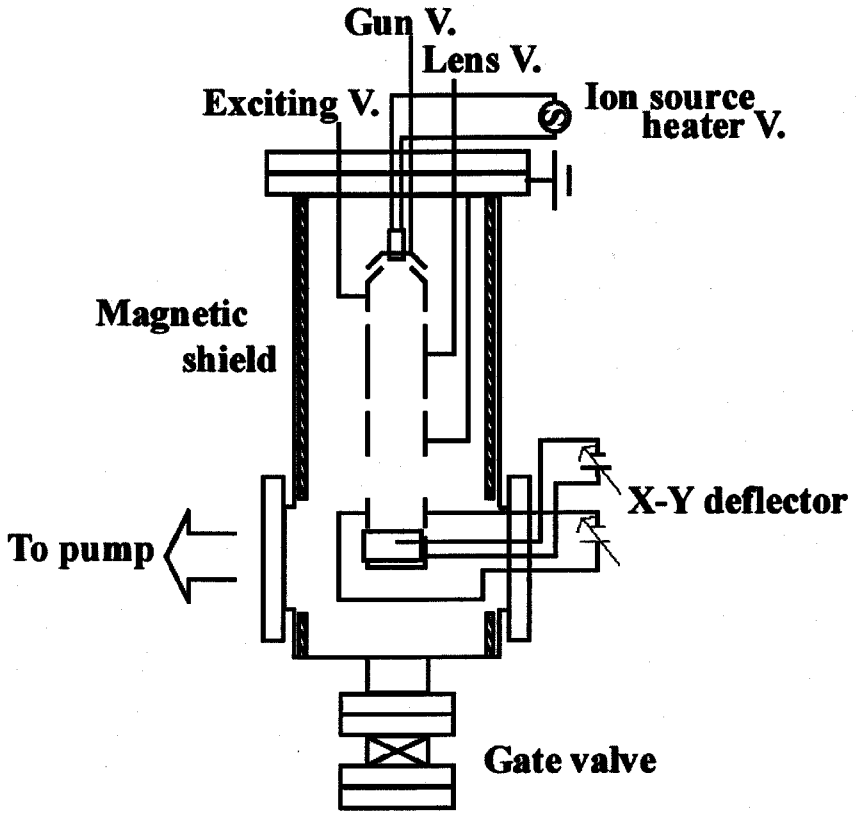

Fig. 3.4 Schematic drawing of the Li beam gun. This gun consists of an ion gun with a Li source, a Pierce extractor and cylindrical lens.

The ion beam is neutralized in the Cs neutralizing cell. Figure 3.5 shows a detail of the cesium neutralizer. The neutralizer is divided into a cesium cell part that stores cesium and a neutralizing cell part that is on the beam way. The neutralizer chamber is wounded by a heater wire and is further covered by aluminum foil as thermal insulation. Its temperature is monitored by a thermocouple and kept at 180 C° during experiments. Cesium in a glass capsule is mounted in the Cs cell part, and the glass capsule is broken by a moveable side bar and cesium is disclosed in the vacuum. This bar is also used as a shutter between the cesium cell and the neutralizing cell. It is opened for several seconds during the timing of plasma discharge. The neutralizer is also covered with magnetic shield made by soft iron plates. The advantage using cesium is that the operation at low temperature is possible compared with lithium or sodium.

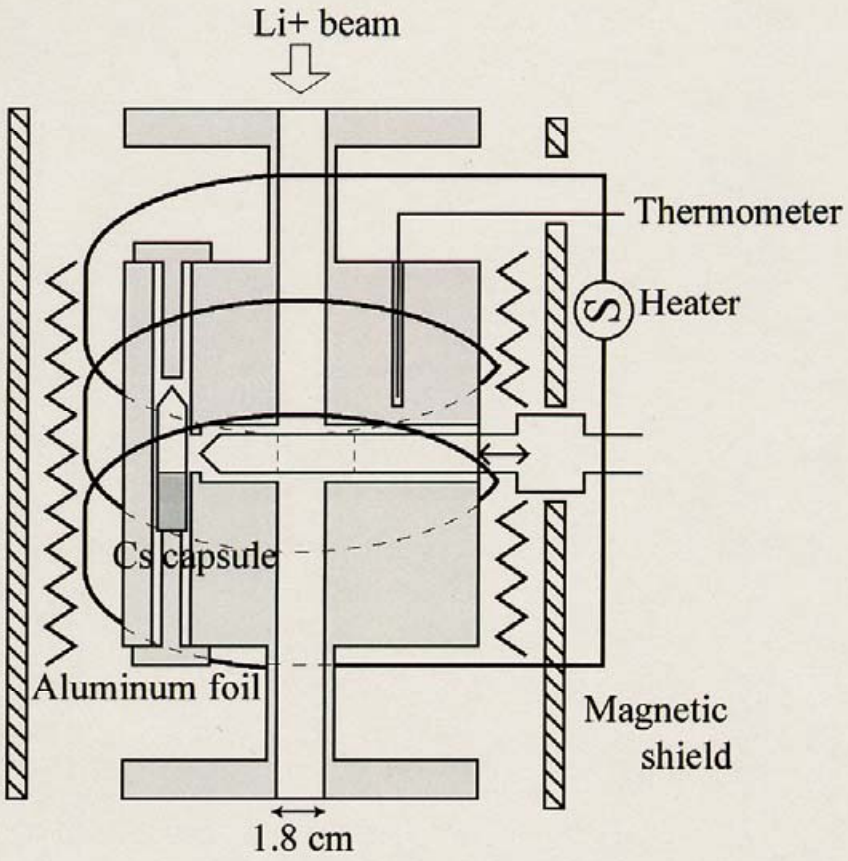

Fig. 3.5 Schematic drawing of the heat pipe type cesium neutralizer.

The spatial resolution is basically determined by the life time of the excited state of Li atom. For the 15 keV beam, the spatial resolution is less than $v_b\tau_{em}$ = 1.7 cm and beam penetration is expected to be about $2x10^{18}$ m^{-2} of line integrated density. For example, when plasma density is 10^{19} m^{-3}, beam penetration depth is 0.2 m. The neutral beam diameter is about 20 mm in the CHS vacuum chamber, which is 2.5 m from the ion gun. A Faraday cup type secondary emission detector is located just below the CHS vacuum chamber to monitor the neutral beam intensity. The neutral current is estimated from this secondary electron intensity assuming the secondary emission coefficient to be unity.

In order to change the beam injection angle, the beam line is mounted on the remote drive mechanism. Since a stray magnetic field exists, a motor with permanent magnet cannot be used. So, a compressed air motor is used. The beam line angle can be changed between -18° and +18° in major radius direction. The position of the pivot is at (x,y) = (1200 mm, 395 mm). The beam injection angle can be controlled remotely at the control room. When the beam angle is 0°, the beam is injected vertically at x = 1200 mm. A picture of the whole beam injection part is shown in Fig.3.6.

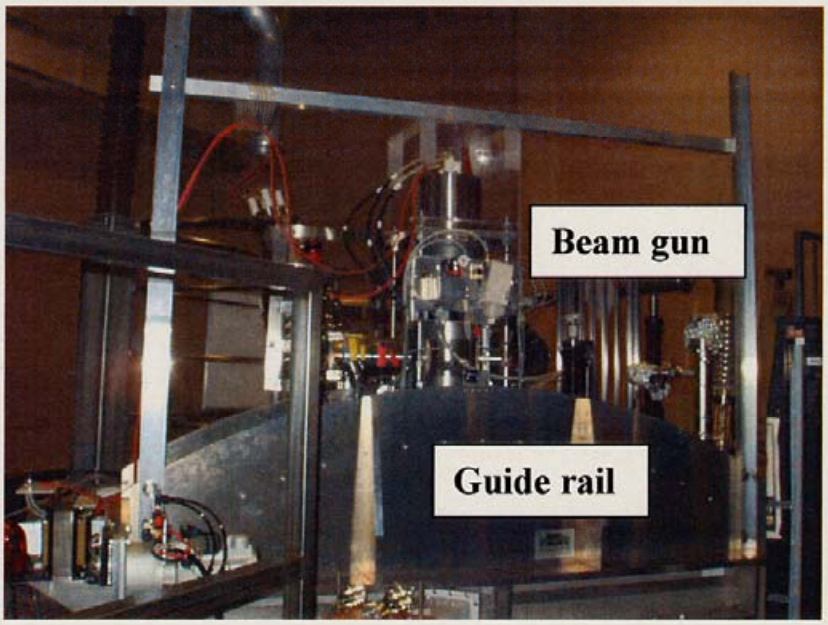

Fig. 3.6 The picture of the whole beam injection part.

The influence of the stray field cannot be disregarded in the CHS upper part. For example, when magnetic axis Rax is 0.921 m and the magnitude of magnetic field is 1.76 T, the stray magnetic field is about 100 G around the gun, which is 2 m above the equatorial plane of the tours. Therefore, lithium ions before neutralized in the neutralizer are easily bent by the stray field. In order to prevent the effect of this stray field, it is necessary to cover the beam injector and the neutralizer by magnetic shield. The injector part is covered by a cylindrical permalloy (2 mm thick, inside diameter 100 mm and permeability 10^5). The neutralizer is covered by electromagnetic soft ion plates (8 mm thick, inside diameter 100 mm and permeability 2000). Shielding coefficient S which is the ratio of the strength of outer magnetic field and inner magnetic field in cylindrical shield is expressed as $S \sim 3t\mu/4r$. Here t is thickness, r is inside diameter and μ is permeability. Then S is about 1600 at the beam injection part and the magnitude of stray field is mitigated to several mm gauss. At the neutralizer part, S is about 120 and the magnitude of stray field is mitigated to several gauss. However, the beam line cannot be covered with magnetic shield ideally. Hole exist in a shield at the location of the vacuum pump, gate valve, movable rod on the neutralizer and so on. From these reasons, actual shielding coefficient is smaller than the calculated value.

It is also necessary to evaluate the influence of the ferro-materials on the CHS magnetic surface structures. Simple evaluation formula has been developed in LHD design study, and this idea is used in our case. In LHD, criterion for introducing ferro-materials is determined so that the irregular magnetic field due to the magnetic shied materials should be less than 10^{-4} of the original field. The irregular magnetic field by on plasma center by the ferro-materials located at (R, z) is estimated by the following formula.

$$\Delta B\ (G) = 1200V\sqrt{[(R-3.9)^3 + Z^3/2]}$$

Here V is the volume of the ferro-materials (m^3), R is the distance from the center of torus (m), and Z is the distance from the equiatorial plane. Since major radius of LHD is 3.9 times as large as that of CHS, scale-down formula by factor 3.9 can be used. In our case on CHS, the magnetic shield material of $V = 0.00197\ m^3$ is located at $R = 1.2$ m

and Z = 1.85 m. Then estimated irregular field strength is ΔB (G) = 0.747 and $\Delta B / B = 0.18 \times 10^{-4}$. In addition, the influence of the magnetic field by the iron rail used for the drive mechanism for the beam injecter is estimated as $\Delta B / B = 0.5 \times 10^{-4}$. Here the same criterion is used in CHS as in LHD. The influence of the magnetic shield materials on the confinement field is less than 10^{-4}.

In order to check the effect of this magnetic shield, the lithium beam is injected into the CHS chamber that is filled with He gas, and the luminescence is observed by a photo-multiplier-tube (PMT). When, there is no magnetic shield, the luminescence signal disappears shortly after energization of coils started (Fig 3.7a). The reason would be that the ion beam is bent by the stray magnetic field before it is neutralized. On the other hand, Fig. 3.7b shows the luminescence signal with the magnetic shield. The luminescence signal recovers at the flat-top phase of the CHS magnetic field. Since stray field strength is large in the start-up and fall-down phase of the magnetic field, the lithium beam is stilled bent. The stray field in these phases is due to irregular vertical fields combination in order to destroy closed magnetic surfaces and to prevent production of run away electrons.

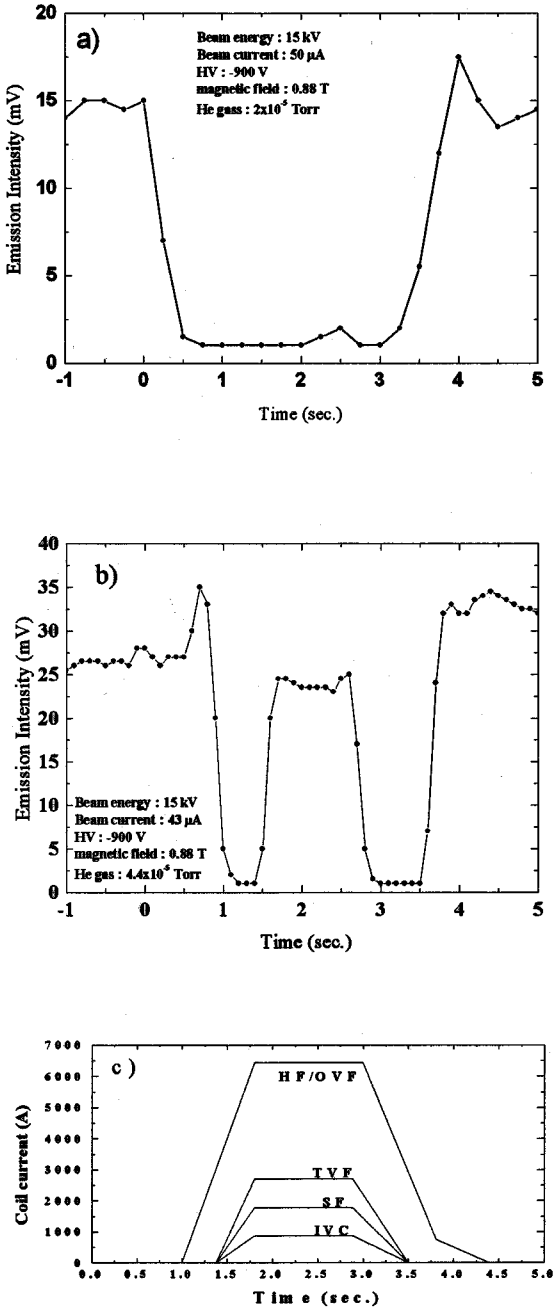

Fig 3.7 Effect of the magnetic shield on the emission signals.

a) Beam emission signal disappears while the CHS coils are excited. (without magnetic shield)

b) Beam emission signal recovers during the phase of flat-top magnetic field. (with magnetic shield)

c) Time sequence of coil currents.

3.2.2 Optical detection part

Light collection optics, which detect the light emission from the LiI resonance line, is located on the side port of the torus (5O port). The optical system consists of a lens, optical fibers, optical interference filters and Avalanche Photodiode (APD) detectors. Figures 3.8 and 3.9 are schematic drawing of the optical system and Figures 3.10 - 3.12 are pictures of the optical system.

The light collection lens has a diameter of 100 mm and focal length f = 179.9 mm. The angle between a sight line and an equatorial plane is 20 degree. Twenty-five couplers for optical fibers are prepared on the light collection lens corresponding to twenty-five observation points along the beam. The coupler is numbered from No.1 to No.25 in an order from the top. The lithium beam is injected from No. 25 observation point. Another way of saying, No. 25 side observes outside of the plasma and No. 1 observes inner side of the plasma. Distance from the coupler No.13 (center channel of couplers) to principal point of the light collection lens is 261.6 mm. The interval of couplers is 4 mm. Spacing of the observation points are from 8.8 mm to 9.6 mm depending on the location. When the beam diameter is 20 mm, the spatial resolutions to magnetic surface near the LCFS are set to from about 10 mm for -18 deg. and 20 mm for -2 deg., respectively. Because the beam and the LCFS cross almost perpendicularly at the beam injection angle of -18 degree, spatial resolution becomes almost the same as the spacing of the observation points. On the other hand, at the beam injection angle of -2 degree, the beam is injected along the LCFS, spatial resolution is determined by the beam diameter.

Eight channel optical fibers can select eight observation points by using eight couplers among those. For each channel, seven fibers (diameter of 1 mm) are packed in a line at the coupler, and the image of the fiber cross section on the beam is roughly 2 mm x 14 mm. Seven fibers are converted into a circle of 3 mm diameter and length of 15 m and are introduced into the filter box. This system is necessary to cope with different plasma positions depending on the position of the magnetic axis. The

transmission efficiency of the optical fiber is about 60 % at 670.8 nm. The light is then made into parallel ray by plane-convex lens (diameter 30 mm, f = 60). The optical interference filter is mounted on this parallel ray region. Then, the light is converged onto the APD with a preamplifier whose frequency response is DC~ 100kHz.

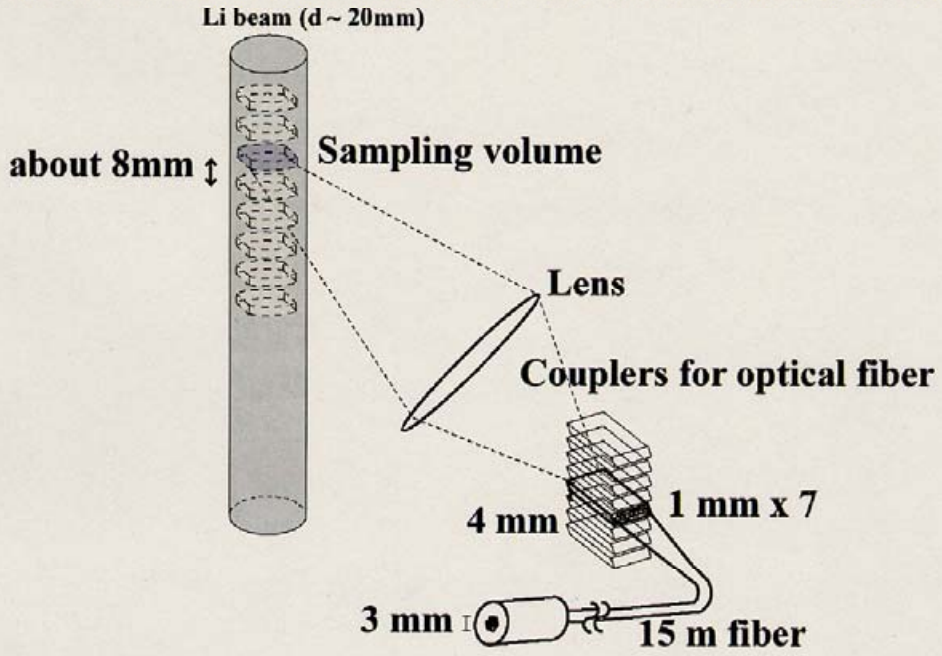

Fig.3.8 Schematic drawing of the light collection optics.

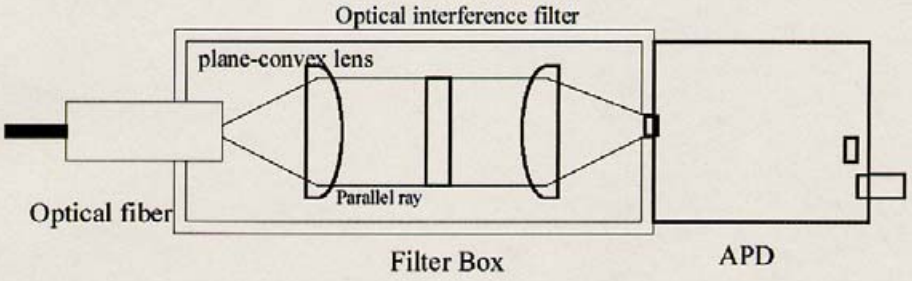

Fig. 3.9 Schematic drawing of the filter Box. Plane-convex lens :diameter 30mm, focal length 60 mm

Optical interference filters : center wavelength of 670.4 nm, bandwidth of 2 nm

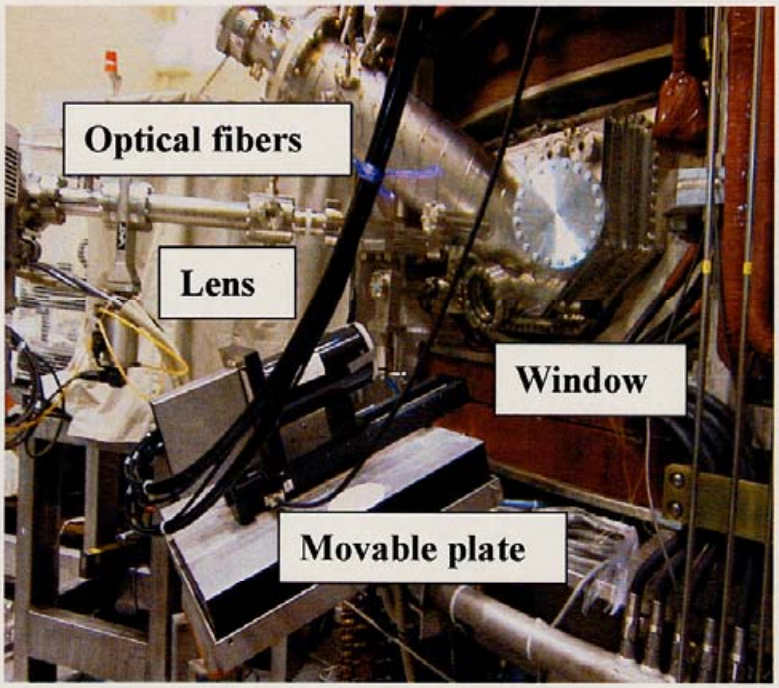

Fig.3.10. The picture of the light collection optics.

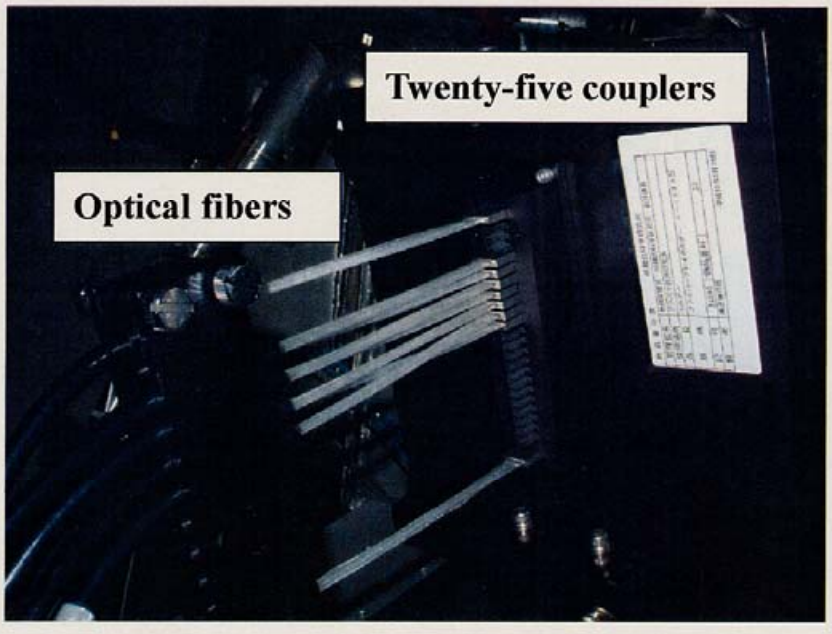

Fig.3.11 The picture of twenty-five couplers and eight channel optic fibers.

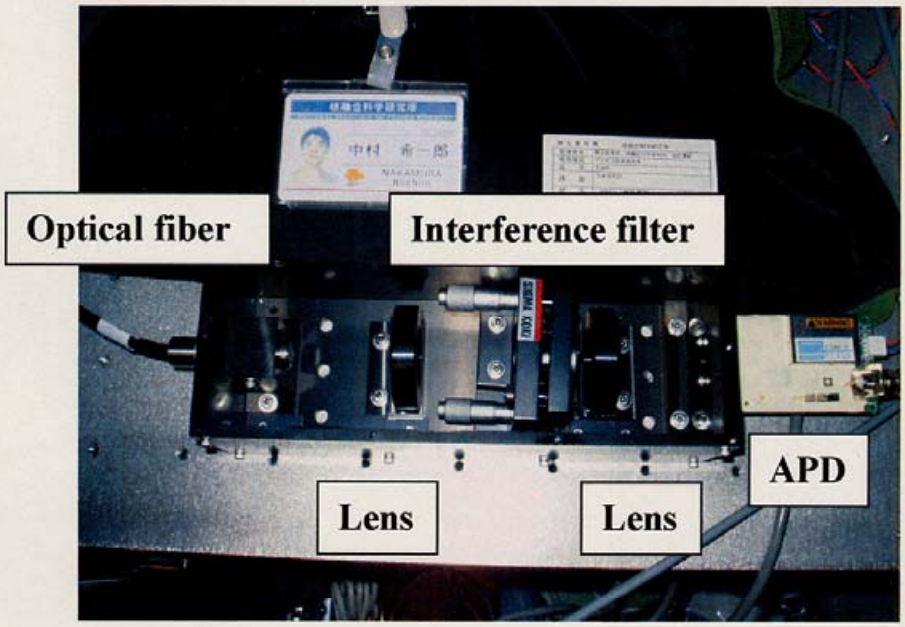

Fig.3.12 The picture of the filter box.

Since the angle between the beam-line and the sight-line is not a right angle, the observed emission suffers Doppler shift. Maximum Doppler shift at beam energy of 15 keV is 0.9 nm in this system. There are two methods to solve this problem. One is to tilt the optical interference filter so that the parallel ray passes the filter at proper angle. The center wavelength λ_θ of optical band pass filter depends on the light incidence angle θ and is described as follows.

$$\lambda_\theta = \lambda_0 [1 - (Ne / N^*)^2 \sin^2\theta]^{1/2}$$

Here, λ_0 is the center wavelength at normal incidence, Ne is refractive index of external medium, which is an air in our case and N* is effective reflective index of the filter. The advantage of this method is that narrow bandwidth of interference filter can be used and effect of spurious emission can be reduced. However, the angle of filter must be changed depending on the beam injection angle. The other method is that the bandwidth of the interference filter is selected wide enough to cover the maximum Doppler shift. The advantage of this method is that the filter angle can be fixed. But the noise level due

to spurious emission would increase in this case.

In our system, the second method is adopted. The optical interference filters are selected with the center wavelength of 670.4 nm, bandwidth of 2 nm and peak transmission of about 65 %. Two-dimensional emission profile is obtained by changing the beam injection angle shot by shot. Shaded area in Fig.3.13 indicates the possible sample volume location determined by the twenty-five optical couplers. Beam-line at 0° injection angle and the sight-line crosses at the point (x,y) = (1200 mm, 0 mm).

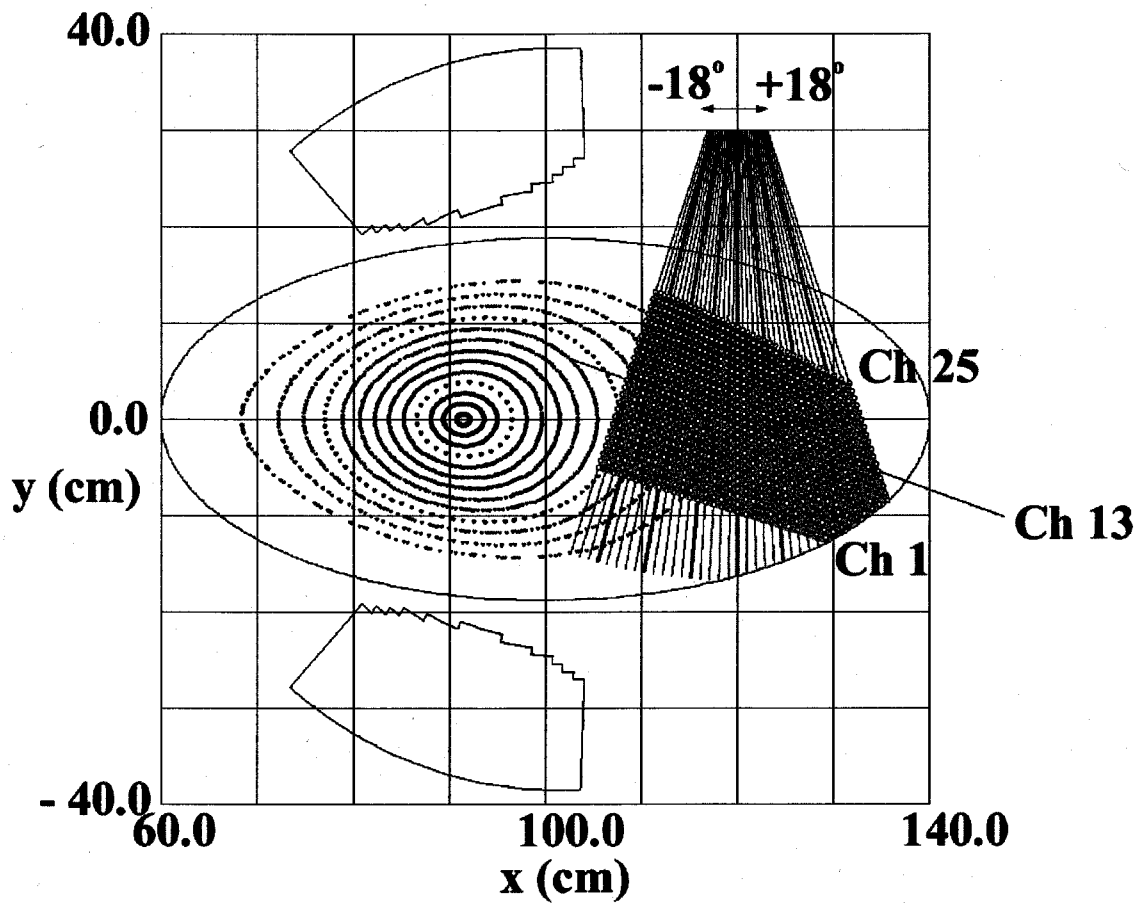

Fig 3.13 Map of the observation area. The magnetic configuration described in this figure shows Rax of 0.92 m.

The signal to noise ratio is less than one (S/N < 1) as shown in Fig 3.14. The upper trace is raw signal from the plasma, where the lithium beam is injected with 100 Hz modulation. It shows that the signal from lithium beam is not clearly recognized in the noise. Lower trace is the signal output from phase sensitive detectors (beam modulation is 4 kHz). Two possible noise components are considered. One is the detector noise (of APD itself) and the other is the background light emission.

In order to see the signal level of LiI emission from the beam, spectral line analysis is carried out using a Czerny-Turner spectrometer with focal length of 50 cm. Spectral line profiles are shown in Fig. 3.15 with the lithium beam (upper traces) and without the beam (lower trace). Three small Gaussian shape spectral lines are the emission signals from the beam with different beam injection angle. A sharp and strong spectral peak is found in both traces, which is identified as a LiI resonance line from the back ground plasma. It is considered that lithium atoms deposited onto the vacuum chamber wall are released into the plasma during the discharge. The intensity of this component increases as time, because our beam injector is not in pulse operation and the beam is injected continuously even between discharge. Pulse operation is being considered, which should decrease this spurious signal. Other remarkable impurity lines are not observed. In order to solve this problem, the signals from APD detectors are introduced to phase sensitive detectors with 4 kHz beam modulation. Time constant of the phase sensitive detection is 3 ms in the present measurements.

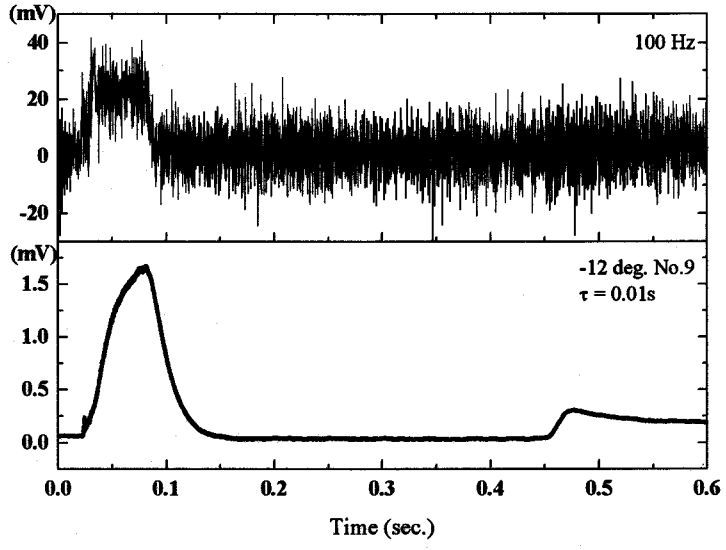

Fig. 3.14 The signal of lithium beam emission. Upper trace is raw signal from the lithium beam injected into the plasma. Lower trace is the signal output from the phase sensitive detectors.

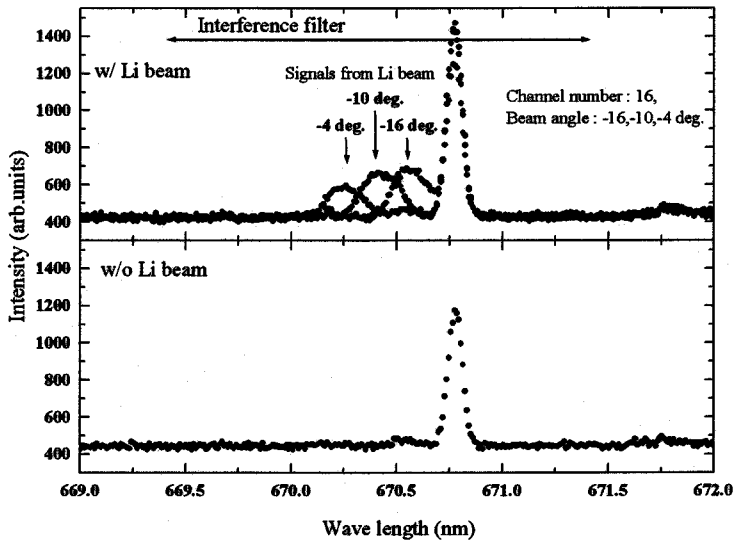

Fig 3.15 Spectral line profiles observed by a Czeruy-Turner spectrometer. Upper traces are with the lithium beam and lower trace is without the lithium beam.

3.2.3 Data acquisition and analysis

The output signals from the phase sensitive detectors are digitized by AD converter and stored temporarily at the local memory of the VME standard. Digital resolution is 3.05×10^{-4} V (-10 V to 10 V) and time resolution is 160 μs when processing data are up to 16ch. Those data are sent to the main data acquisition computer system named "int" and then is displayed on the terminal computer "inf6". The raw data are displayed on the monitor immediately after the discharge. After the experiment, the whole data is transferred and analyzed at a personal computer (PC). The flow of this data processing is shown in Fig 3.16.

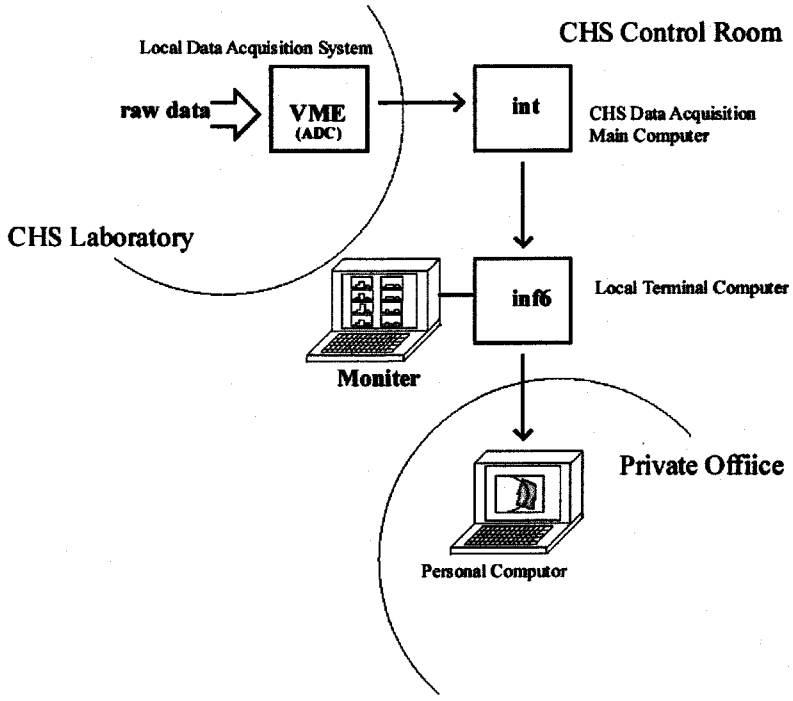

Fig 3.16 Flow chart of data acquisition and processing.

3.2.4 Calibration

Since the Li beam intensity and the beam profile can change slowly with time, calibration of relative sensitivity between channels is preferred to be carried out shot by shot. In standard CHS operation, a hydrogen puff (killer puff) is introduced to prevent high-energy electron production during the turn-off phase of the helical coils. If the neutral gas spreads uniformly within CHS chamber for a short time, the calibration between channels can be attained for every shot by using the emission signal of the Li beam due to collision with hydrogen gas. However, afterglow plasma may disturb the uniform nature of the hydrogen gas. The hydrogen gas density is about 10^{18} m^{-3} - 10^{19} m^{-3}. Afterglow plasma still remains when killer puff is introduced, but its density is about 10^{16} m^{-3}. Moreover, the electron temperature is as low as several eV at most. Based on these facts, it is considered that the influence of afterglow plasma is small and the injected hydrogen neutrals can not be ionized. Considering the amount of neutral hydrogen, the gas density distribution becomes uniform in the CHS chamber in a short time. Then in-situ calibration of the relative sensitivity between channels is possible.

3.3 Experimental results

Experiments have been carried out for the inboard limiter configuration, where the magnetic axis is at R_{ax} = 0.921 m and the magnetic field strength is 0.95T on the axis. Hydrogen plasmas are produced by electron cyclotron resonance (ECR) heating with a gyrotron of 53 GHz and 170 kW. Neutral beam injection (NBI) heating is additionally applied using the two beam lines (both in co-direction) with 40 keV and total power of 1.3 MW.

3.3.1 Measurement of Steady state plasmas

First, steady state plasmas are measured. Plasma is produced by ECH and heated by two NBIs. ECH is applied from t = 20 ms to 120 ms and NBI from t = 80 ms to 180 ms, where t = 0 is the start of data acquisition for diagnostic instruments. Plasma density is controlled by preprogrammed gas puff system. The average electron density in the ECH phase is about $1x10^{19}$ m^{-3} in the present experiment. The average electron density in the NBI phase depends on the heating schemes and is $4x10^{19}$ m^{-3} in this experiment. The core electron density profiles measured by the YAG laser Thomson scattering show flat and parabolic profiles in ECH and NBI plasmas, respectively.

The measurements are carried out in shot by shot bases with changing the Li beam injection angle in the major radius direction. Observation areas for two different operations are shown in Fig.3.17. The area A is near the LCFS and the area B is outside of it. These measurements are performed on the separate day. Therefore, plasma parameters for the two cases are not necessarily the same.

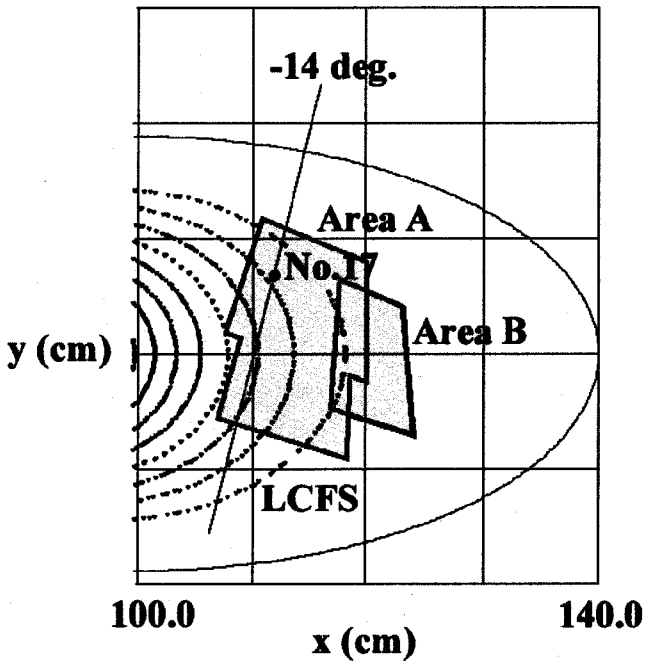

Fig. 3.17 The map of observation areas. Near and outside of LCFS is covered.

Figure 3.18 shows example of light emission from the LiI resonance line for channel 17 and the beam line injection angle of -14 degree (the observation point is indicated in Fig.3.13). Since the signal level is almost constant both during ECH phase and NBI phase, emission intensity averaged over 20 msec is used for 2D mapping shown later. It is noted that remarkable increase of the emission intensity at NBI is primarily due to the increase of electron density near the LCFS. Signal from a killer puff, which is introduced to prevent high-energy electron production during the turn-off phase of the helical coils, is also detected at around t = 450 msec. Expanded signal at this phase is shown in the same figure. The emission signal comes from the collision with neutral hydrogen gases. Since the hydrogen gas distribution becomes uniform in a short time, relative sensitivity between channels can be calibrated during the shot.

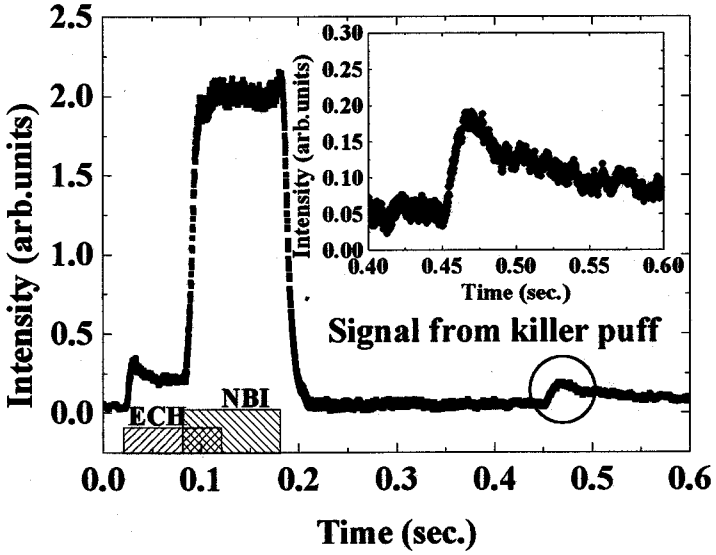

Fig. 3.18 An example raw data of light emission signal of the LiI resonance line taken at the Channel No. 17 with the beam injection angle of -14 deg. (See the beam line and the channel position shown as a dot in Fig.3.17). An inserted figure is an enlargement of the signal from the killer puff.

Figure 3.19 shows sample spatial distribution of the beam emission intensity for ECH and NBI plasmas along the injected beam path with injection angle of -14 degree. The lithium beam is injected from the large channel number side. Those data are obtained from the three discharges with the same condition, because our detector system has only 8 channels at the moment. Beam attenuation is observed both in ECH and NBI phase.

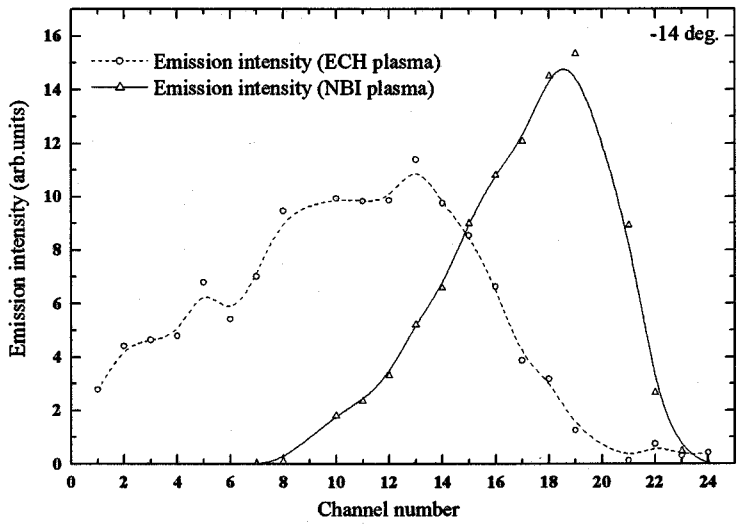

Fig. 3.19 Spatial distribution of the beam emission intensity for ECH and NBI plasmas along the injected beam path with injection angle of -14 degree.

Electron density is reconstructed from this emission profiles. When the plasma density is large, full emission intensity distribution is measured. Then the density profile can be reconstructed using the beam attenuation method. For example, at NBI plasma shown in the Fig. 3.19, emission intensity decreases completely near the channel No.7. The density profile of the 0th order is first calculated using eq. (2.18). Then more accurate density profile is calculated iteratively using eq. (2.19) and effective rate coefficients given by the 0th order density profile. Figure 3.20 shows the electron

density of NBI plasma at -14 degree using the beam attenuation method. The broken line shows the 0th order density distribution and the solid line shows the density distribution reconstructed after 5 times iteration. In this method, density profile is found to be converged comparatively quickly. The reconstructed density loses accuracy at inner region of the plasma. In this study, it is reasonable to consider that this reconstruction method can be adapted in the region from the edge to the position where emission intensity becomes 70 % of its peak.

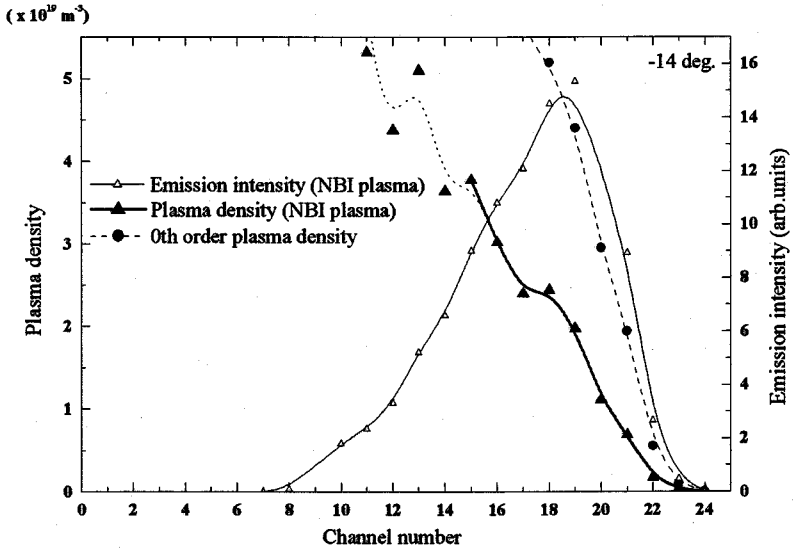

Fig. 3.20 Electron density profile reconstructed by the beam attenuation method. The broken line shows the 0th-order density profile and the solid line is the result after 5 times iteration.

When the emission profile is not measured completely within an observation range, the beam intensity method is used to reconstruct the electron density. In this method, gas calibration is necessary, in principle, to derive the value of sensitivity of the optical system as described in section 2.2.3. However, the density distribution is already calculated by the beam attenuation method for NBI plasma in this experiment, this sensitivity calibration can be skipped.

In the region that plasma density is small and beam attenuation is negligible, the electron density is calculated form the eq. (2.13). Then, the electron density is proportional to the beam emission intensity. Here the constant α can be determined experimentally from the data in the region of low density. Figure 3.21 shows the relation between the electron density and the beam emission intensity in low density region. Data points in this figure are obtained from the data set for NBI plasma with beam injection angle from -18 degree to -12 degree.

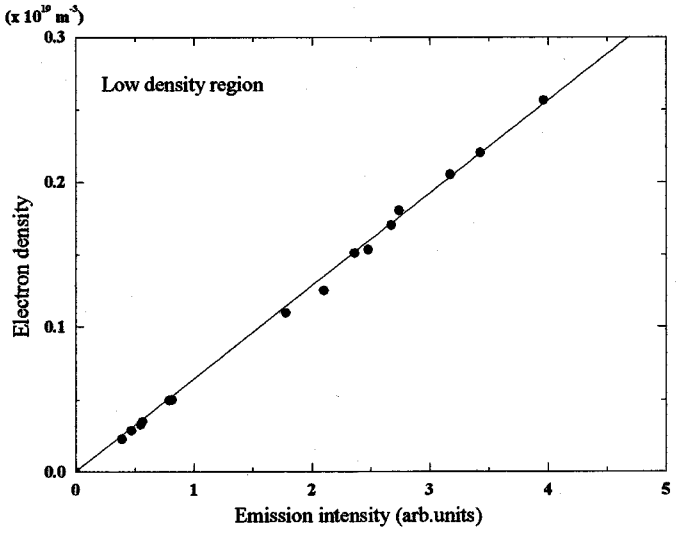

Fig. 3.21 Relation between emission intensity and electron density at low density region

The electron density is derived by the beam intensity method as described in section 2. Figure 3.22 shows the electron density of ECH plasma at -14 degree using the beam intensity method. The broken line shows the density distribution to be used an initial value and the solid line shows the density distribution which is reconstructed by taking the beam attenuation into account. The reconstructed density loses accuracy at inner region of the plasma. This is because only a few percent experimental error or accuracy of the atomic data affect the reconstructed density profile when beam attenuation is severe.

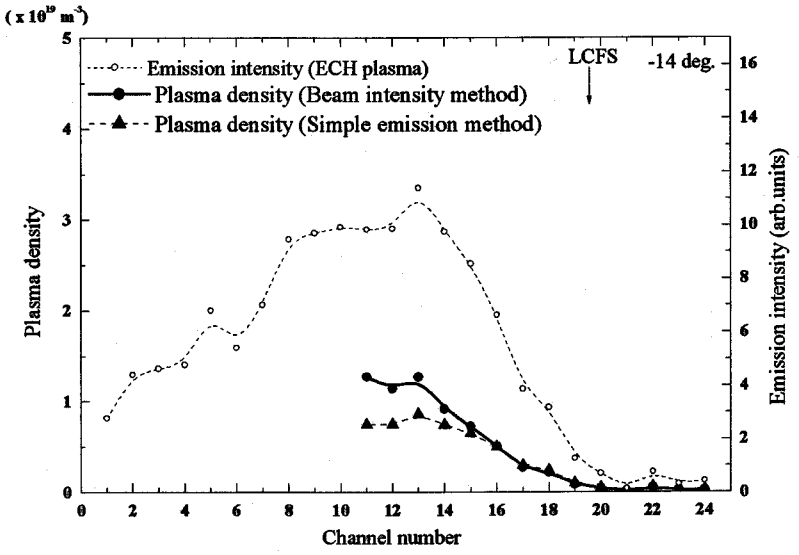

Fig. 3.22 Electron density profile reconstructed by the beam intensity method with iteration. Broken line shows the density profile from the simple emission method.

In this study, the adaptation range in the beam attenuation method is fixed in the region from the edge to the position where emission intensity becomes its peak. The beam intensity method can be applied for the plasma density up to $2x10^{19}$ m^{-3}, which is determined in comparison with the beam attenuation method. It should be noted that the accuracy of calibration also influences the reconstructed density. In the higher density region above $2x10^{19}$ m^{-3}, the reconstructed densities by the two methods deviate quickly as shown in Fig. 3.23.

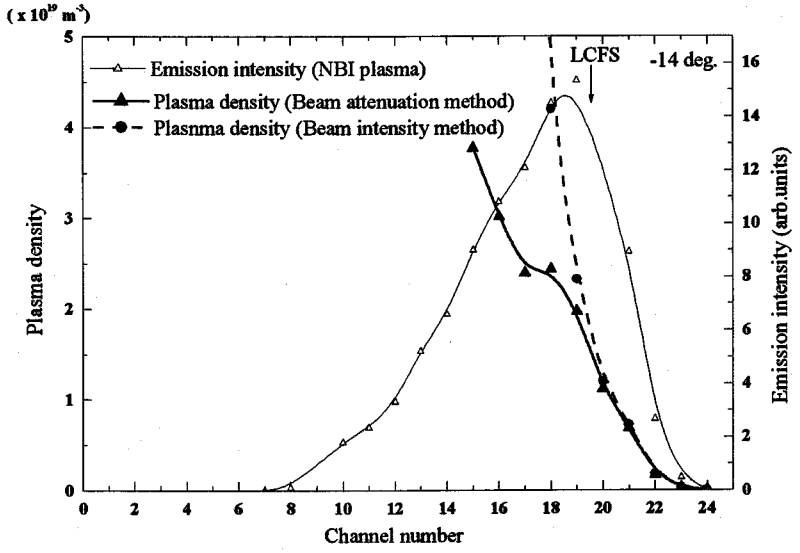

Fig.3.23 Comparison of the beam intensity method with the beam attenuation method. Both profiles are in good agreement in the edge region of the density up to $2x10^{19}$ m^{-3}.

Two-dimensional profiles of the beam emission intensity near the LCFS (area A) are shown in Fig. 3.24(a) for the ECH phase and Fig. 3.24(b) for the NBI. Smooth contour of the emission intensity along the LCFS is observed in the ECH phase. However, the contour is shifted roughly by 2 cm downward because of the time of flight of the lithium particles. The contour deviates from the flux surfaces in the core region, which is due to beam attenuation. The peak of the beam emission intensity roughly follows the LCFS in NBI phase and rapidly decreases toward the core, suggesting higher density plasma within the LCFS. It is also noted that plasmas are clearly observed outside the LCFS and that those plasmas are spreading in the direction of the separatrix region.

Two-dimensional profiles of the electron density are reconstructed from the data shown in Fig. 3.24, which are shown in Fig. 3.25(a) for the ECH phase and Fig. 3.25(b) for the NBI. Here, density profiles of ECH plasma are derived by beam intensity method and density profiles of NBI plasma from -18 deg. to -6 deg. of the injection angle are derived by the beam attenuation method and those from -4 deg. to 0 deg. are derived by the beam intensity method. The contour lines in the figures are the magnetic surface for $\rho = 0.837 \sim 1.171$, and the thick line is for $\rho = 1.0$ (LCFS). In Fig 3.25(a), it is noted that the influence of time of flight is taken into account, namely, the whole density distribution is shifted by 1.7 cm in the beam injection direction. Equi-density contours coincide the magnetic surfaces inside of the LCFS. While, in Fig 3.25(b), significant amount of plasmas are observed even outside of the LCFS.

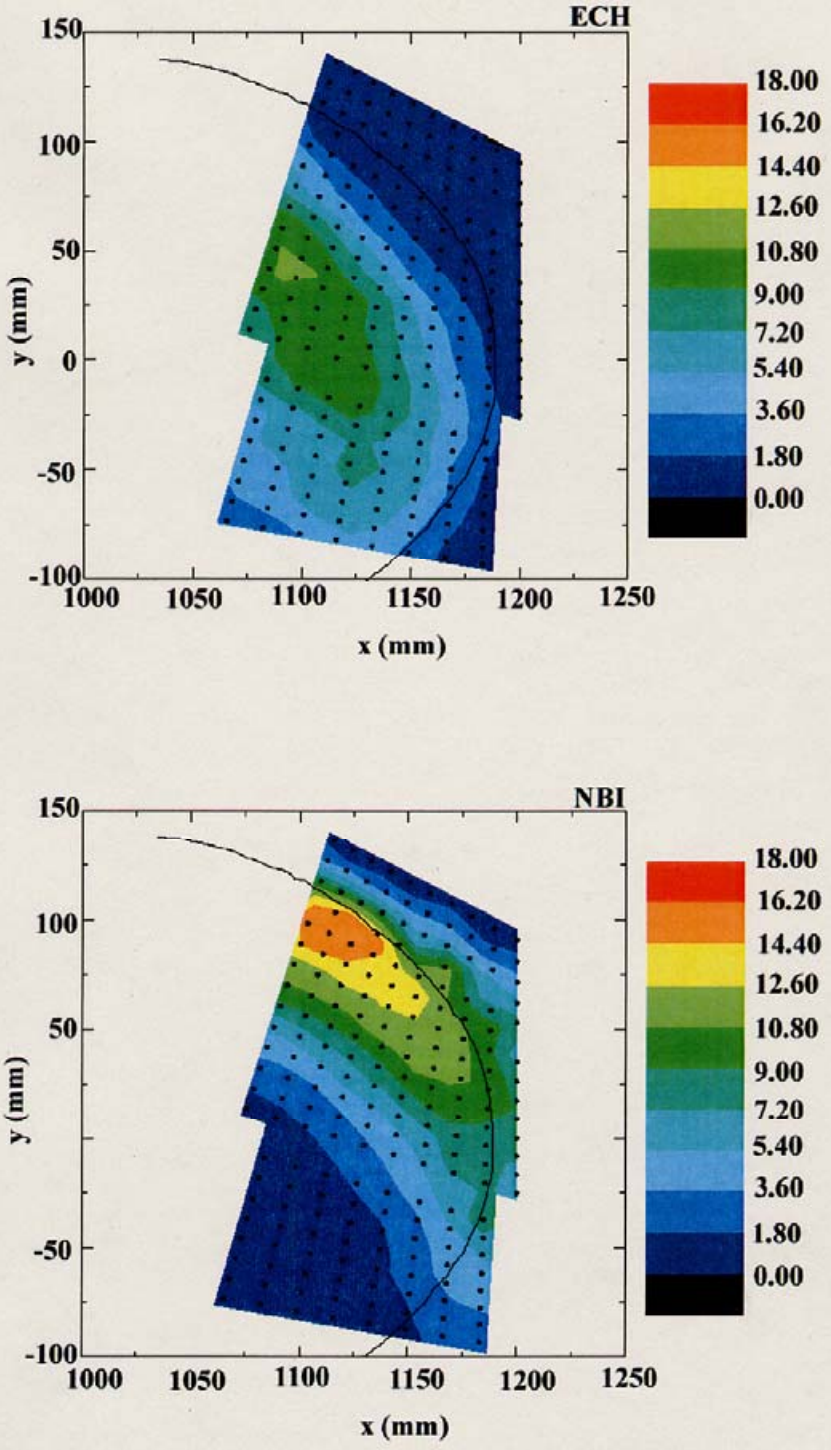

Fig 3.24 Two-dimensional profiles of the beam emission intensity for (a) ECH plasma and (b) NBI plasma. (Observed in area A shown in Fig.3.13.)

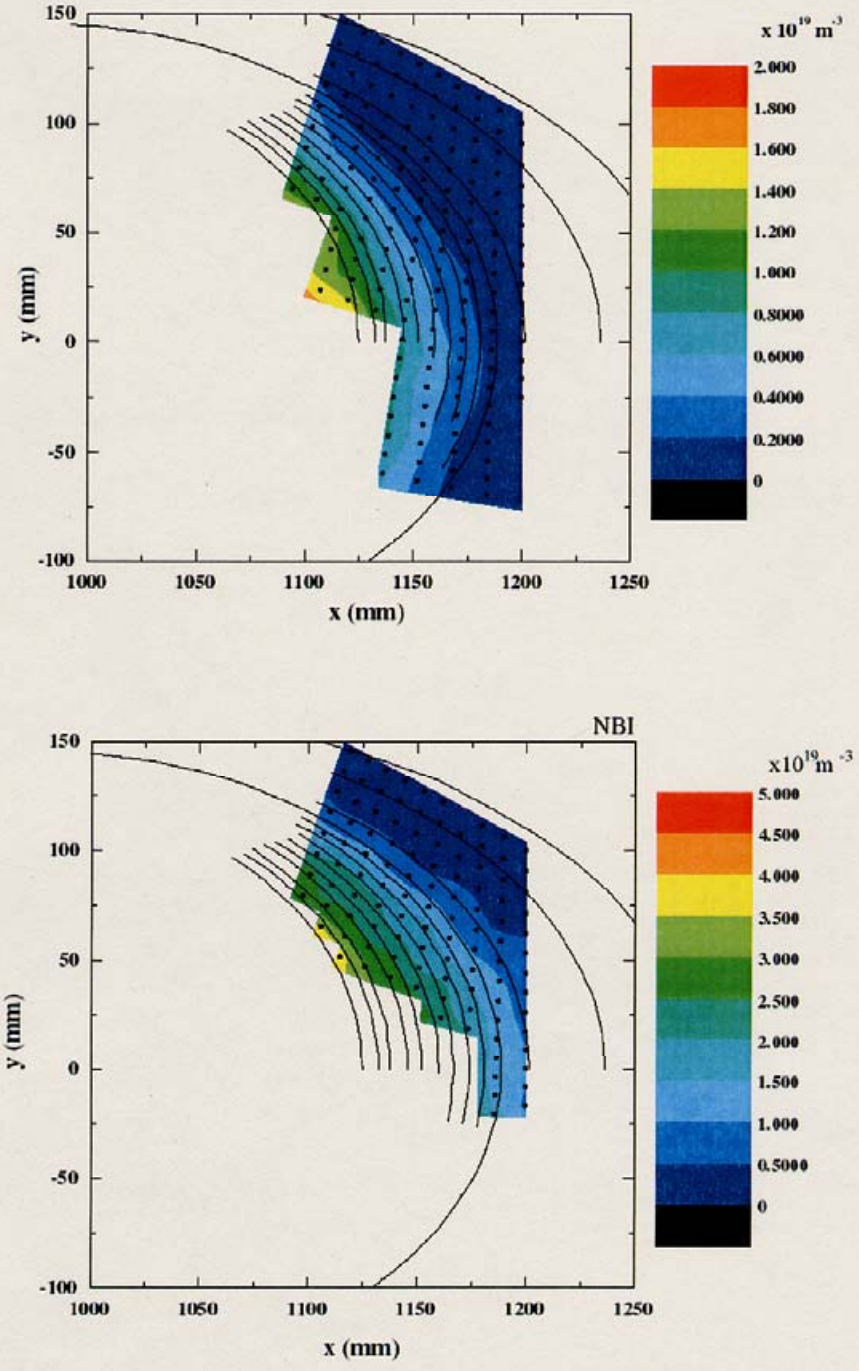

Fig 3.25 Two-dimensional profiles of the electron density reconstructed from the data in Fig.3.24 for (a) ECH plasma and (b) NBI plasma.

In order to see the relation between the electron density and the average minor radius ρ the data set obtained above are re-plotted. Figures 2.26(a) and 3.26(b) show the electron density profiles as a function of ρ along the four different beam injection chords for the ECH plasma and for the NBI plasma, respectively. It is shown that the electron density inside of the LCFS for ECH plasma is a good function of the minor radius ρ. It is consistent with the two dimensional map of the electron density shown in Fig. 3.25(a). As for the NBI plasma, the electron density is well described as a function of the minor radius even outside of the LCFS. It suggests that the influence of the magnetic surface still remains outside the LCFS in spite of the inboard limiter configuration. Then it is reasonable to plot an average electron density using the two-dimensional data as a function of ρ, which is shown in Fig. 3.27. Data points are the superposition of the data in Fig. 3.26(a) and 3.26(b). Real plasma boundary appears to exist around $\rho = 1.10$ for NBI plasma.

Next, measurements are extended to outer region (area B). Two-dimensional map of the beam emission intensity for the NBI phase and ECH are shown in Fig. 3.28, which is obtained in the similar discharge condition before but different day. It should be noted that surface plasma structure is reflecting the magnetic field structure outside of the LCFS even in the inboard limiter configuration. Figure 3.29 shows the two-dimensional electron density profiles at ECH phase and NBI phase, which is consistent with the observation before. At NBI phase, it is again shown that plasma spreads outside the LCFS toward the separatrix region. It is noted that effect of time of flight is not include in the figures.

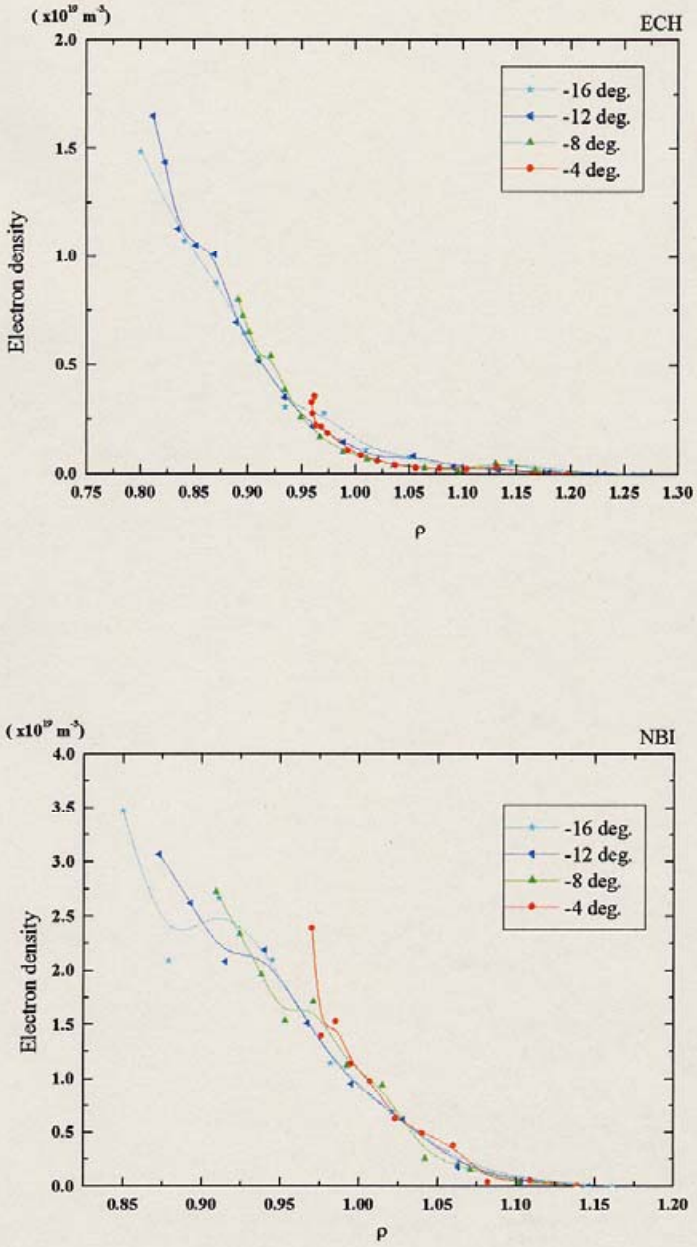

Fig.3.26 The relation between average minor radius ρ and the electron densities at the beam angle of -16 deg. -12 deg. -8deg. and -4 deg. for (a) ECH plasmas and (b) NBI plasmas.

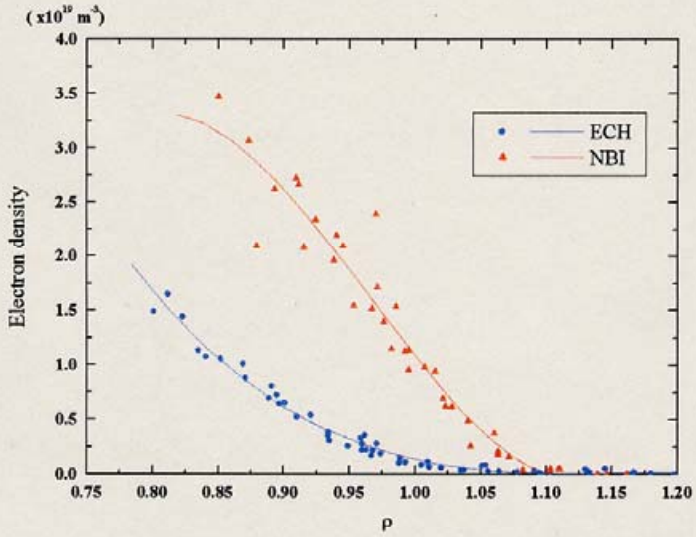

Fig.3.27 The relation between ρ and the electron densities for ECH plasma and NBI plasma.

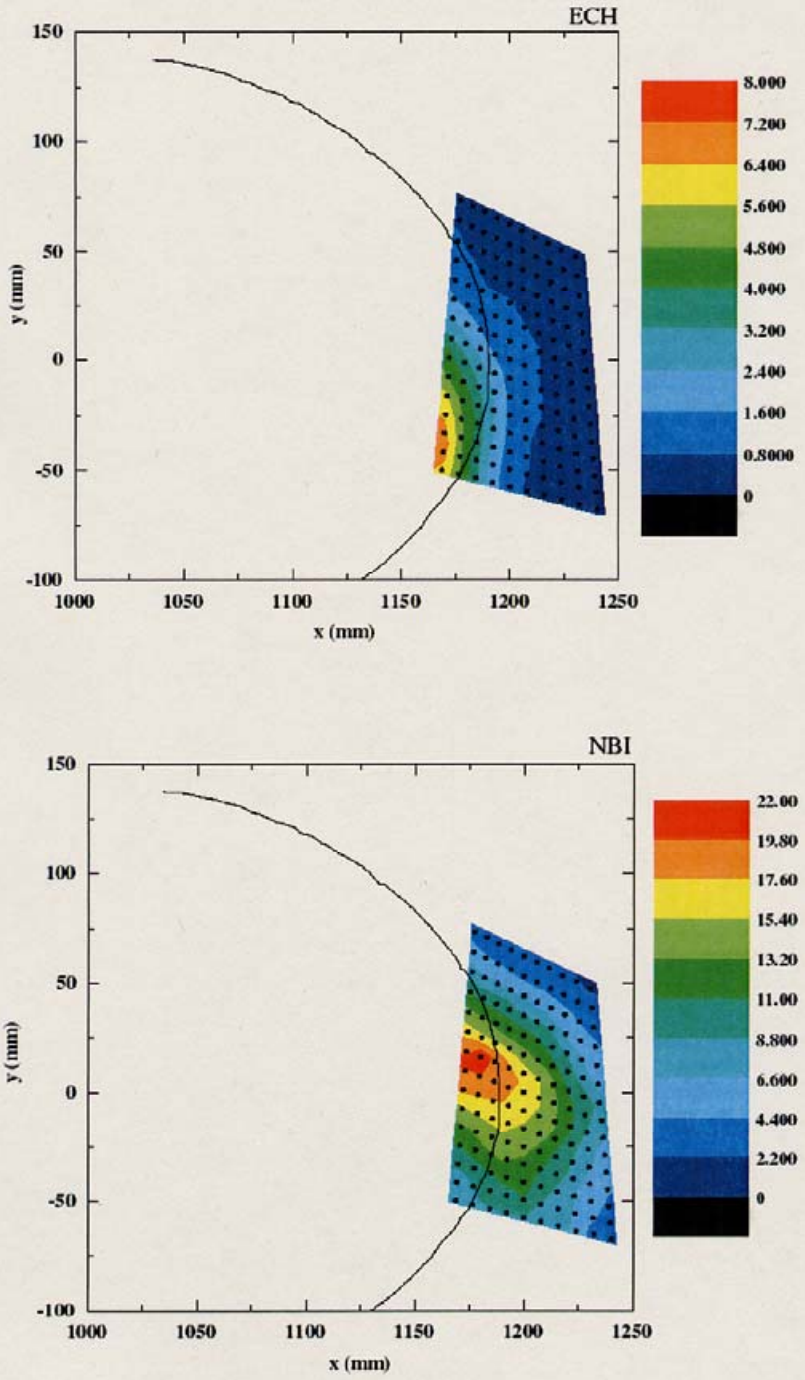

Fig 3.28 Two-dimensional profile of the beam emission intensity outside of the LCFS in (a) ECH plasma and (b) NBI plasma. (Observed in area B shown in Fig.3.17)

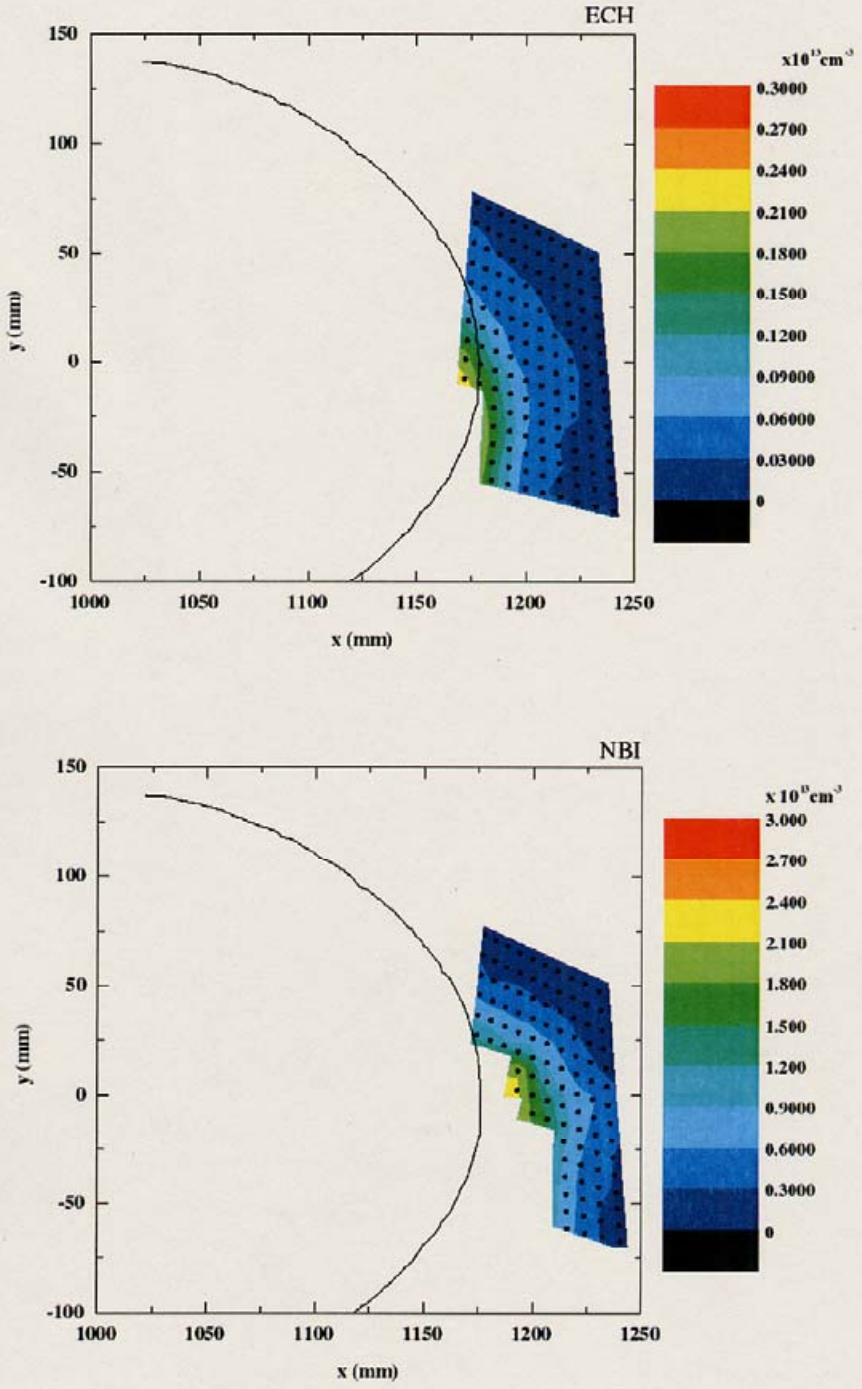

Fig.3.29 Two-dimensional profile of the electron density reconstructed from the data in Fig.3.28 for a) ECH plasma and b) NBI plasma

3.3.2 Plasma with ETB formation

Edge electron density profiles are measured in the discharges with the edge transport barrier (ETB) formation. Figure 3.30 shows the discharge scenario. ECH is applied from t = 20 ms to 50 ms to produce plasma. Then NBI#1 is injected into the ECH target plasma from t = 32 ms to 132 ms and the secondary NBI#2 is added from t = 72ms to 102ms. The H_α emission signal drops several ms after the NBI#2 injection. The increase of the edge density at the transition is confirmed by means of YAG laser Thomson scattering, indicating the formation of ETB similar to the standard H-mode discharges.

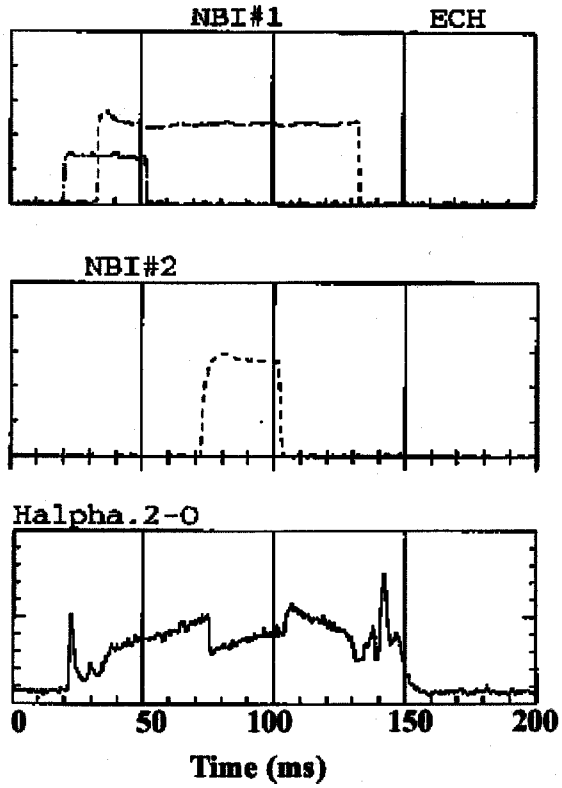

Fig. 3.30 Traces of plasma heating scenario and Hα emission signal.

Figure 3.31 shows a sample raw signal of the Li emission, where the beam injection angle is -16 deg. and the detection channel number is No.17. It shows that emission signal decreases quickly at the transition phase and it recovers at the end of the transition. Figure 3.32 shows the emission intensity profiles along the beam with injection angle of -16 deg. It shows clearly that emission intensity profiles shift outward during the ETB formation.

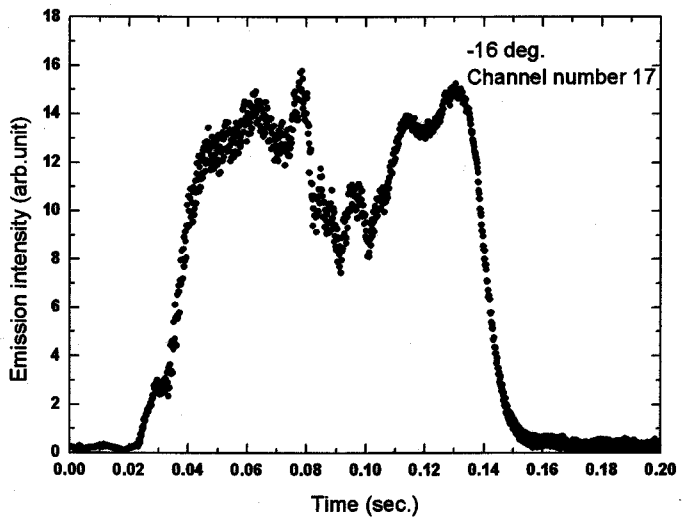

Fig. 3.31 LiI emission signal for the discharge with ETB. (-16 deg. Channel No.17)

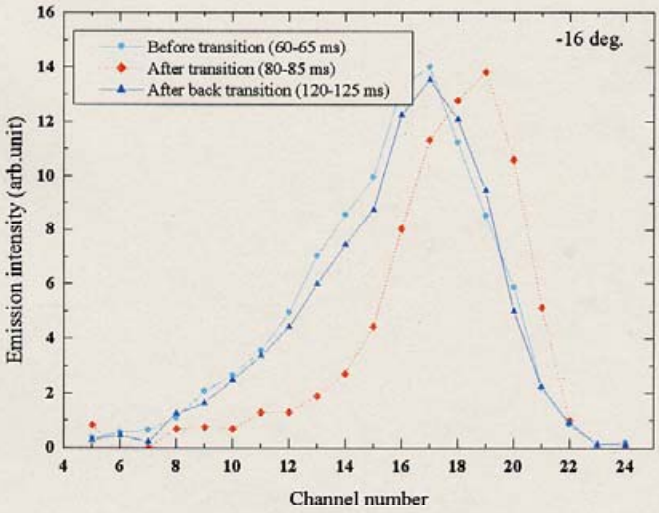

Fig.3.32 Emission intensity profiles along the beam with injection angle of −16 deg. The position of LCFS is around channel No.20.

Two-dimensional profiles of electron density before and after the transition are shown in Fig. 3.33(a) and Fig. 3.33(b), respectively. Change of the density profiles is confirmed also in 2D profile data. Figure 3.34 shows the electron density profiles before (t = 70 ms) and after the transition (t = 80 ms) as a function of the average minor radius ρ. Data points are obtained from several shots with different beam injection angle It is shown that density profiles become steep during the ETB formation just inside the LCFS.

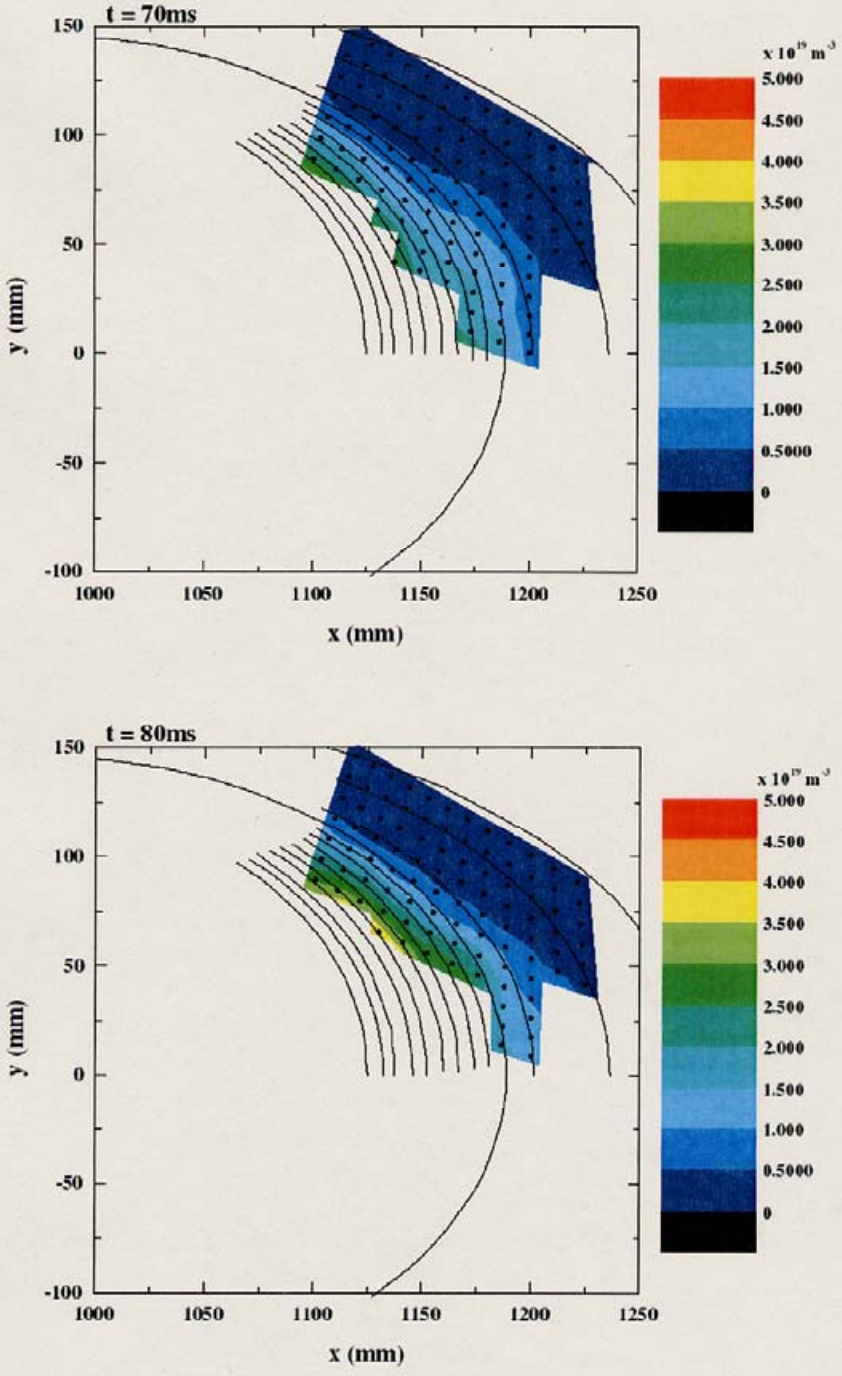

Fig. 3.33 Two dimensional map of electron density.

a) t =70ms (before transition)

b) t=80ms (after transition)

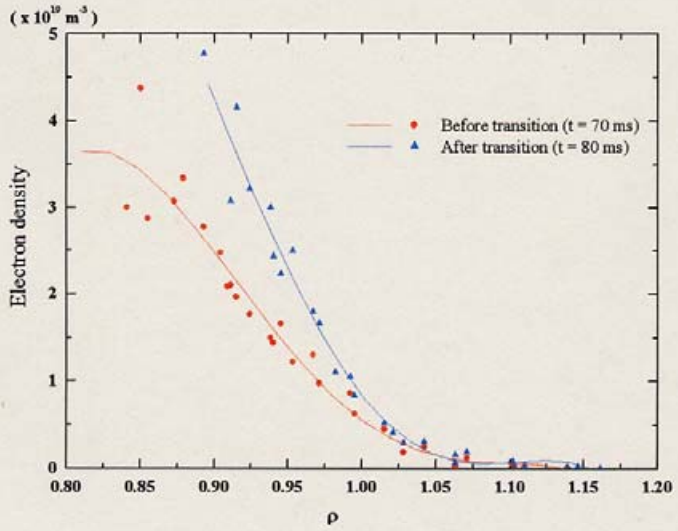

Fig. 3.34 The density profiles before and the after transition.

4. Discussions and Summary

In the previous section, several examples of two dimensional electron density profile measurement in the edge and separatrix region of helical device CHS using the lithium neutral beam probe are introduced. This is the first demonstration of two-dimensional diagnostic of density profiles with LiBP. There still remain several issues to be improved, which will discussed below.

Relative sensitivities between channels are calibrated by detecting signals at the killer puff phase, where the LiI emission signals are caused by collisions with uniformly filled neutral hydrogen gas (in-situ calibration). This method makes us free from monitoring the absolute value or gradual change of the beam intensity during the day. Actually it is not easy to measure the beam intensity accurately under the magnetic field circumstances. On the other hand, because of rather small signal level at the killer puff phase in the present experiments, the calibration data fluctuate by 10% at maximum shown in Fig.4.1. It shows the relative sensitivity between the channels obtained from the signal from the killer puff. Data point for each channel is normalized by the data of channel No.1 and the error bar is one standard deviation. It is obtained from a series of 24 shots data.

Fluctuation of the relative sensitivities is the major source of error in the determination of the 2D beam emission profiles. In order to reduce it, we are planning to introduce helium gas using additional gas puff system. Since helium gas is not absorbed in the vacuum chamber wall, larger amount of gas can be injected as a killer puff without disturbing plasma density control in CHS experiments. In addition, an ion gauge to measure the absolute pressure or neutral helium number density is under preparation. Then it is possible to determine the absolute electron density even if the full beam emission profile is not obtained.

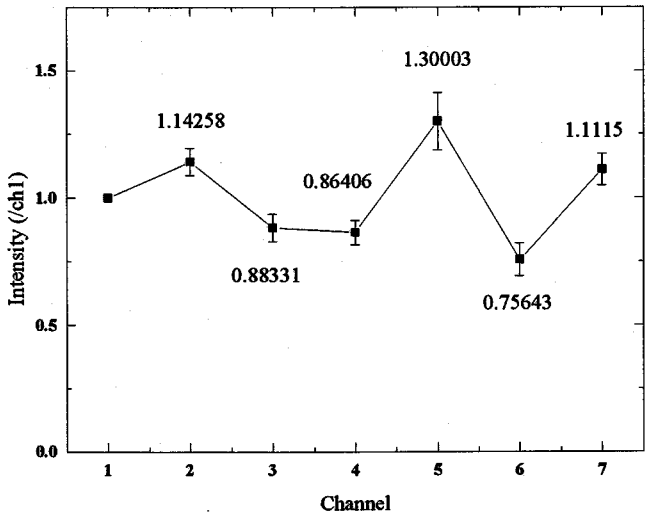

Fig. 4.1 Relative sensitivity between the channels. It is obtained from the signal at the killer puff.

The spatial resolution is determined by the effective lifetime of the lithium 2p state. When collision is rare, it is roughly $v_b\tau$, which is 1.7 cm for 15 kV beam. This time of flight affects the shift of the observation point. The observed shift of the emission profile contour near the LCFS in ECH phase is found to be consistent with the estimation. On the contrary, in the higher density NBI phase plasma, multiple processes become important due to more frequent collisions, making the effective lifetime shorter. Then the spatial resolution should be better and the shift of the emission profile should be shorter. This effect was estimated in detail by McCormick et al. using a collisional-radiative model for the atomic processes, and the result showed that the spatial resolution is 0.5 cm or less even for higher energy beam of 30-70 keV [4.1]. Such calculation is not done yet for our data, but it is reasonable to shift the whole density distribution by 1.7 cm in the beam injection direction in ECH plasma, and to assume similar shortening of the spatial resolution in NBI plasmas. The 2D electron density profiles for NBI plasma shown here do not include the shift of the observation

point due to time of flight. The effect of this shift should be considered depending on the density for more detailed discussion.

On CHS, electron temperature becomes less than 10 eV outside of the LCFS at NBI plasma [4.2]. For example, when electron density is $1x10^{18}$ m^{-3}, the value of the emission rate coefficient for 5 eV plasma becomes about 66% of the value for 20 eV plasma. In the low electron temperature region, detailed Te profile measurement is necessary, which is not possible with LiBP only. Collaboration with other diagnostic is under discussion. Then density profile reconstruction will be improved.

The reconstructed electron density at the LCFS agrees with that roughly estimated from the core density profile measured by the Thomson scattering and the line integrated density by the 2 mm interferometer. Effects such as due to effective Z are not included in the present analysis. In the classical model [4.3,4], higher charged states have larger cross section for charge transfer. For example, if the impurity ion is assumed to be O^{6+} (typical impurity species in CHS [4.5]), and Z_{eff} of 2.5 (that means the ratio of the O^{6+} density to the electron density ratio is 0.05), ionization rate coefficients $<\sigma_{ip}v_{r\text{-}e}>$ and $<\sigma_{is}v_{r\text{-}e}>$ increase by 30 % compared with the case of Z_{eff} =1 (no impurity). The effect of impurity would modify the absolute value of the electron density, but it is less than 10 %.

The experimental data suggests that the ECH plasma is confined inside the LCFS, so plasmas with density above 10^{18} m^{-3} do not exist outside of the LCFS. In contrast, the NBI plasma is spreading toward the separatrix region and noticeable amount of plasma is confined in this ergodic region even though in the inboard limiter configuration. The plasma with the density of 10^{19} m^{-3} exists even 4 cm apart from the LCFS along the equatorial plane. On the CHS, the field line length just outside the LCFS is about 3 m, because the rotational transform $\iota / 2\pi$ is almost unity at this area and there are four mirror structures. A part of plasma that escapes to outside LCFS is trapped in those mirrors. Therefore it is considered that the plasma is not necessarily lost immediately, even though magnetic configuration is inboard limiter one. Comparison of plasma structure in this region between the limiter configuration and the magnetic limiter

configuration is planned near future. These studies will be useful for actual design of the diverter in the heliotron type devices.

Since the beam current is presently in the range of 0.05-0.1 mA with the 6 mm diameter ion source and the phase sensitive detection method is adopted, the time response is limited to 3 ms at the moment. Improvement of the signal to noise ratio is necessary to extend the time response by removing the phase sensitive detection. For that purpose, it is necessary to develop the source that is derived larger current. Actually, a 10 mA class lithium beam with a larger diameter β-eucriptite source has been developed by D. Thomas and is used for fluctuation study up to 100 kHz range [4.6]. Compromising a larger size ion gun with the movable beam injector system is under planning to extend our diagnostic to MHD study around the LCFS. Moreover, development of the larger beam current also opens the way of the application to current distribution measurement by Zeeman effect, ion temperature measurement by charge exchange and impurity concentrations.

In summary, the LiBP for two-dimensional diagnostic of edge plasmas has been developed and installed on the CHS. The beam injection angle can be varied and the beam can cover the edge and separatrix region of helical diverter configuration. Two-dimensional electron density profiles are obtained near and outside of the LCFS for ECH and NBI heated plasmas, suggesting new knowledge on the edge plasma structures in the heliotorn type helical device. Significant amount of plasmas are observed outside of the LCFS near the separatrix region in NBI plasmas even in the inboard limiter configuration. Two dimensional density profiles are measured before and after the ETB discharge. It is confirmed that the edge density profiles change during the ETB formation transition. The density profile data near the edge region is essential to understand the physical pictures of ETB in stellarators. The 2D-LiBP is one of the promising diagnostic in this field, although further improvement of beam injector, calibration method as well as the density profile reconstruction using collisional-radiative model is necessary.

5. References

Chapter 1

1.1 F. Wagner, et al, Phys. Rev. Lett. 49, (1982) 1408

1.2 K. Toi, et al, Phys. Rev. Lett. 64 (1990) 1895

1.3 Toi. K et al, Plasma Physics and Controlled Nuclear Fusion Research 2 (1993) 461

1.4 Erckmann V et al, Phys. Rev. Letter 70 (1993) 2086

1.5 H. M. Mott-Smith and I. Langmuir Phys. Rev., 28 (1926) 727

1.6 K. Takiyama, Y. Kamiura. T. Fujita, et al., Jpn. J. Appl. Phys. 26 (1987) 1945

1.7 K. Kawasaki, K. Takiyama, and T. Oda, Jpn. J Appl. Phys. 27 (1988) 83

1.8 K. Takiyama et al., Rev. Sci. Instrum. 59 (1988) 2351

1.9 M. Wickham, S. Fornaca, N. H. Lazar, et al., Rev. Sci. Instrum. 55 (1984) 1748

1.10 K. Kadota, C. Takahashi, H. Iguchi et al., Rev. Sci. Instrum. 56 (1985) 857

1.11 W. P. West, D. M. Thomas, E. S. Ensberg, et al., Rev. Sci. Instrum. 57 (1986) 1552

1.12 C. Honda et al., Rev. Sci. Instrum. 58 (1987) 1593

1.13 H. Yamaoka, K. Kadota, H. Yamai, et al., Rev. Sci. Instrum. 59 (1988) 115

1.14 J. C. Hosea et al., Phys. Rev. Lett. 30 (1973) 839

1.15 D. G. Nilson and D. N. Hill, Rev. Sci. Instrum. 68 (1997) 1195

Chapter 2

2.1 H. P. Eubank, P. Noll, and F. Tppert, Nucl. Fusion 5, (1965) 68

2.2 F. C. Jobes, J. F. Marshall, and R. L. Hickok, Phy. Rev. Lett. 22 (1961) 1042

2.3 J. C. Hosea, F. C. Jobes, R. L. Hickok, and A. N. Dellis, Phy. Rev. Lett. 30 (1970) 839

2.4 J. Fujita and K. McCormick, Proc. 6th EPS

2.5 K. Kadota, K. Tsuchida, Y. Kawasumi, and J. Fujita, Plasma Phys. 20, (1978) 1011

2.6 H. Iguchi, K. Takagi, K. Takasugi, T. Shoji, M. Hosokawa, M. Fujiwara, and K. Ikegami, Rev. Sci. Instrum. 56 (1985) 1056

2.7 K. McCormick, H. Murman, and M. El Shaer, J. Nucl. Mater. 121 (1984) 48

2.8 K. McCormick and ASDEX team, Rev. Sci. Instrm. 56 (1985) 1063

2.9 A. Pospieszczyk, F. Aumayr, H. L. Bay, E. Hintz, P. Leismann, Y. T. Lie, G. G. Ross, D. Rusbuldt, R. P. Schweer, and H. Winter, J. Nucl. Mater. 128&129 (1989) 574

2.10 J. Schweinzer et al., Plasma Phys. Control. Fusion 35 (1992) 1173
2.11 S. Zoletnik, S. Fieldler, G. Kocsis, K. McCormick, J. Schweinzer and H. P. Winter, Plasma Phys. Control. Fusion 40, (1998) 1399
2.12 K. McCormick, S. Fiedler, G. Kocsis, J. Schweinzer, and S. Zoletnik, Fusion Engineering and Design. 34-35 (1997) 125
2.13 M. Ueda, H. Iguchi, S. Sasaki and J. Fujita, J. Nucl. Mater. 196-198 (1992) 923
2.14 S. Sasaki, S. Takamura, M. Ueda, H. Iguchi, J. Fujita, and K. Kadota, Rev. Sci. Instrum. 64, 1699 (1993).
2.15 T. Morisaki, et al,. J. Nucl. Mater. 241-243 (1997) 977
2.16 A. M. Howald, J. M. McChesney, and W. P. West, Rev. Sci. Instrum. 66, 312 (1995).
2.17 M. Brix, A. Korotkov, M. Lehnen, P. Morgan, et al.: to be published in Proc. EPS Conf. on Controlled Fusion and Plasma Physics, (2001)
2.18 T. Morisaki, A. Komori, O. Motojima, and LHD Experimental group Rev. Sci. Instrum. 74, 1865 (2002).
2.19 D. M. Thomas, Rev. Sci. Instrum. 66, (1995) 806
2.20 D. M. Thomas, Rev. Sci. Instrum. 74, (2003) 1541
2.21 J. P. Blewett and E. J. Jones Phys. Rev. 50(1936) 464
2.22 M. Ueda, R. R. Silva et. al. J. Phys D Appl. Phys. 30(1997) 2711

Chapter. 3

3.1 K. Matsuoka et al., in Plasma Physics and Controlled Nuclear Fusion Research 1988, vol. 2, IAEA, Vienna (1989) 411
3.2 K. Matsuoka et al., J. Plasma Fusion Res. Series, vol. 1 (1988) 30
3.3 S. Okamura et al., Plasma Physics Reports, vol. 23 (8) (1997) 640
3.4 K. Kawahata, et al., Rec. Sci, Instrum. 70 (1999) 707
3.5 K. Tanaka et al., Proc. 26th EPS Conference (1999)
3.6 K. Narihara, T. Minami, et al., Rev. Sci. Instrum. 66 (1995) 4607
3.7 S. Nishimura, K. Ida, et al., J. Plasma Fusion Res. SERIES, 1 (1998) 370
3.8 Toi. K et al. Plasma Physics and Controlled Nuclear Fusion Research 2 (1993) 461
3.9 Erckmann V et al. Phys. Rev. Letter 70 (1993) 2086
3.10 K. Toi et al, 19th IAEA Fusion Energy Conference, Lyon, 2002, EX/S3-2
3.11 S. Okamura et.al, J. Plasma Fusion Res. 79 (2003) 977

Chapter. 4

4.1 K. McCormick, S. Fiedler, G. Kocsis, J. Schweinzer, S. Zoletnik, fusion Engineering and Design 34-35, 125 (1997).

4.2 K. Ohkuni et al. Phys. Plasmas, 8, 4035 (2001)

4.3 R. E. Olson, J. Phys. B: 13 (1980) 483

4.4 H. Ryufuku, K. Sasaki, and T. Watanabe, Phys. Rev. A.21 (1980) 745

4.5 S. Sasaki, S. Takamura, M. Ueda, H. Iguchi, J. Fujita, and K. Kadota, Rev. Sci. Instrum. 64, (1993) 1699.

4.6 D. M. Thomas, Rev. Sci. Instrum. 66, 806 (1995).

6. Acknowledgement

I wish to express special thanks to Dr. H. Iguchi, of National Institute for Fusion Science (NIFS), whose thoughtful supervision provided continuing guidance for this work. I thank Dr. T. Morisaki of NIFS, Dr. M. Ueda of INPE, Brazil and Dr. S. Sasaki of Toshiba Co. for their encouragement and discussion throughout this work.

I acknowledge the encouragement given by Dr. A. Shimizu, Dr. M. Isobe, Dr. C. Takahashi, Dr. S. Nishimura, Dr. C. Suzuki, Dr. Y. Yoshimura, Dr. K. Nagaoka, Dr. T. Minami, Dr. K. Ida, Dr. S. Okamura, Dr. K. Matsuoka and also the all CHS group members at NIFS.

I would like to thank Dr. M. Y. Tanaka and Dr. S. Yoshimura of NIFS.

I would like to appreciate Dr. A. Okamoto, Mr. H. Nakano, Mr. S. Ohshima and also all successive roommates.

I am grateful for desk works managed by official staff ; Mr. K. Matsuura and Ms. S. Urushihara who are in charge of The Graduate Univ. for Advanced Studies at NIFS.

I must give immense thanks to my parents. Their support during the doctoral course was of immeasurable value to me.